SIMULATIONS OF UNSTEADY FLOW PHENOMENA IN CROSS-FLOW TURBINES

by

Mukul Dave

A dissertation submitted in partial fulfillment of
the requirements for the degree of

Doctor of Philosophy

(Mechanical Engineering)

at the

UNIVERSITY OF WISCONSIN–MADISON

2022

Date of final oral examination: 12/14/2022

The dissertation is approved by the following members of the Final Oral Committee:
Jennifer A. Franck, (Advisor) Assistant Professor, UW–Madison, Engineering Physics
Riccardo Bonazza, Professor, UW–Madison, Engineering Physics
Mario Trujillo, Professor, UW–Madison, Mechanical Engineering
Wenxiao Pan, Associate Professor, UW–Madison, Mechanical Engineering
Jinlong Wu, Assistant Professor, UW–Madison, Mechanical Engineering

ॐ श्री गणेशाय नमः।

ॐ श्री सरस्वत्यै नमः।

Acknowledgements

I begin by thanking my parents and my brother for always pushing me to aim higher, my grandmother for her unending love, my wife for being a source of calm and strength as I navigated the final years of my doctoral program, and my in-laws for their positive attitude towards my education. I am blessed to have a loving immediate and extended family as pillars of support through thick and thin.

My advisor, Prof. Jennifer Franck, has been a mentor in the true sense of the word, actively guiding me through this journey. I sincerely thank her for being extremely patient with my style of working and long personal vacations while consistently pushing me to develop all aspects of my professional skill set. I am grateful to the committee members for their encouraging words and constructive feedback. I am indebted to all my teachers and mentors who've led me to this point. I must thank the support staff in the ME and EP departments, especially Dina Christenson, Katherine Wegner, and Sara Hladilek, who made it possible to navigate the administrative and academic aspects of my degree.

I am grateful to have had two wonderful labmates, Bernardo Ribeiro and Kate Lyons, during the initial years of my PhD as they became my circle of support. The more junior graduate students, Trevor Dunt, Riley Bridges, Sara Hartke, Soundarya Ramasubramanian, and Rithwik Kandukuri, continued this camaraderie within the lab. The silly discussions and walks to the cafe made it much easier to get through the work day.

I truly cherish my friendships from before my PhD program who continue to be there for me when needed. I am also grateful for the friends I made during my time at UW-Madison. Looking forward to the next dinner party, cricket match, performances, and umpteen other events drove me through day, week, and semester. I must specially mention my roommate, Nitesh Arora, and Bhagyashree Prabhune for their companionship through the PhD years. Finally, working with the teams at the Indian Graduate Students' Organization,

Saaz, and Hindu YUVA motivated me outside of work and taught me to manage multiple commitments.

I would like to thank my collaborators, co-authors, and peers from the research community. Student members from our lab - Alejandro Calvet, Arianne Spaulding, Hanqi Dong, and Vineet Pasumarti - assisted parts of my research. Tom Derecktor, Steven Winckler, and Michael Miller at Blusource Energy motivated and drove the work on oscillating foil propulsion which does not feature in this thesis but was an important start to my doctoral program. Our collaborators at the University of Washington - Abigale Snortland, Aidan Hunt, Ari Athair, Benjamin Strom, Prof. Brian Polagye, Isabel Scherl, and Prof. Owen Williams - provided valuable experimental data and inputs for my work on cross-flow turbines. Prof. Karen Mulleners and Sébastien Le Fouest at EPFL have also helped improve the quality of my culminating work through stimulating discussion. I am grateful to all of them for inspiring and helping me in continuously moving forward with my research. Lastly, I acknowledge award No. DE-AR0001441 from the Advanced Research Projects Agency-Energy (ARPA-E) for partially funding my PhD research.

Abstract

Cross-flow turbines (CFT) harvest energy from wind or water currents via rotation about an axis perpendicular to the flow, and are a complementary technology to the more common axial-flow turbine. During the 360 degree rotation, the CFT blades experience a cyclical variation in the angle of attack and velocity relative to the oncoming flow, leading to flow separation and reattachment, otherwise known as dynamic stall. This causes an instantaneous loss in torque generation and unsteady force fluctuations which pose a challenge to accurate models and predictions of both the performance and the flow field.

This work first examines the dynamic stall process and resulting wake features of CFTs under confined configurations applicable to river and tidal currents. High fidelity large-eddy simulations (LES) of a straight-bladed two-blade cross-flow turbine operating at a moderate Reynolds number are compared to unsteady Reynolds-averaged Navier-Stokes (RANS) simulations. The RANS model is shown to be sensitive to confinement at the simulated tip speed ratio as it over-predicts power generation due to suppression of flow separation. Results are compared with an unconfined configuration for which the RANS model successfully predicts a power curve, however displays significant differences in the evolution of flow structures.

Next, the stall development is investigated via proper orthogonal decomposition (POD) of the velocity fields from LES. The POD modes' time development coefficients capture the trend of aerodynamic loads on the blade, along with critical events such as vortex formation and detachment. Flow curvature, history effects, and flow induction are identified as significant factors changing the blade aerodynamic loads as compared to pitching or plunging foils.

Lastly, a previously optimized intracycle control of angular velocity that enhances power generation by 40% is compared to constant velocity control. This is enabled by a delay in the blade stall and an alignment of peak torque with the peak of blade angular velocity.

Contents

Nomenclature

A	=	projected area of the turbine normal to the flow
A_ω	=	amplitude of sinsusoidal variation of ω
a_m	=	time development coefficient for mode m
c	=	chord length of the turbine blade
C_m	=	coefficient of pitching moment about the quarter-chord location from leading edge
C_n	=	coefficient of normal force on the blade
C_P	=	power coefficient or conversion efficiency of the turbine
$\overline{C_P}$	=	average power coefficient
C_Q	=	normalized value of torque or torque coefficient
F_n	=	normal force on the blade
k	=	turbulent kinetic energy or sub-grid scale (SGS) kinetic energy
M	=	pitching moment on the blade about the quarter-chord location from leading edge
$\overline{p}$	=	mean component of pressure
$\tilde{p}$	=	spatially filtered pressure
q	=	torque applied to the turbine by the fluid
R	=	outermost radius of the turbine
Re	=	Reynolds number based on blade chord length and freestream velocity
S	=	planform area of the blade
$\boldsymbol{U_\infty}$	=	freestream velocity
$\boldsymbol{U_n}$	=	relative flow velocity (in the reference frame of the blade)
U_n^*	=	non-dimensional magnitude of the relative flow velocity
$\overline{\boldsymbol{u}}$	=	mean component of velocity vector
u'	=	fluctuating component of velocity vector about the time-averaged mean
$\tilde{u}$	=	spatially filtered flow velocity

$\boldsymbol{V}_\omega$	=	linear velocity of the blade
y^+	=	dimensionless wall distance
α_n	=	apparent angle of attack of the flow (in the reference frame of the blade)
α_p	=	preset pitch angle of the blade relative to the tangential direction of its motion
Δy	=	wall-normal distance
θ	=	azimuthal angular position of the blade
λ	=	tip speed ratio
λ_{ci}	=	swirl strength
ν	=	kinematic viscosity of the fluid
ρ	=	density of the fluid
$\boldsymbol{\tau}$	=	Reynolds or SGS stress tensor
ϕ_ω	=	phase shift between θ and sinusoidal variation of ω
ψ_m	=	spatial velocity distribution for mode m
Ω	=	vorticity
ω	=	angular velocity of the blade
$\overline{\omega}$	=	mean of sinusoidal variation of ω

1 Introduction

1.1 Motivation

Increasing the proportion of power generation from renewable energy requires exploring multiple sources in addition to wind and solar energy, such as water currents. According to a recent report on marine energy in the U.S. [1], there is a technical power potential of $220\,\mathrm{TWh/year}$ to be harvested from tidal currents, $99\,\mathrm{TWh/year}$ from river currents, and $49\,\mathrm{TWh/year}$ from ocean currents, which is largely unexploited. These sources have a potential of generating power for remote communities in proximity to the site of power generation where wind or solar energy generation is not feasible and the larger power grids have not reached. As is also the case for wind energy, decentralized power generation in urban areas or remote communities reduces transmission losses and removes dependency on the grid [2].

The most common wind and water turbine design is the axial-flow turbine (AFT), whose axis of rotation is aligned with the flow as shown in figure 1.1a. AFTs have undergone significant technological development and have a large presence in wind energy. An alternative to AFTs are cross-flow turbines (CFT), shown in figure 1.1b and figure 1.3. CFTs

(a) An axial-flow tidal turbine [3].

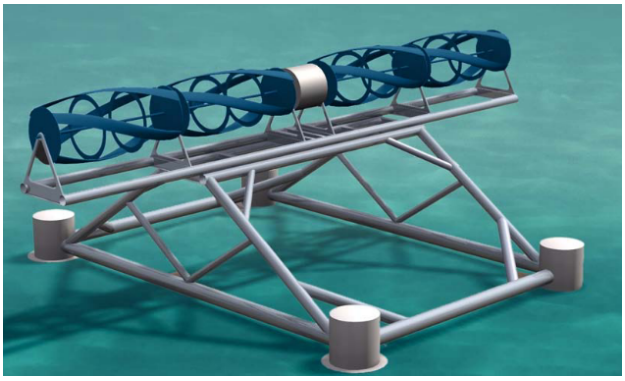

(b) An illustration of cross-flow tidal turbine design [4].

Figure 1.1: Tidal turbines with differing axes of rotations.

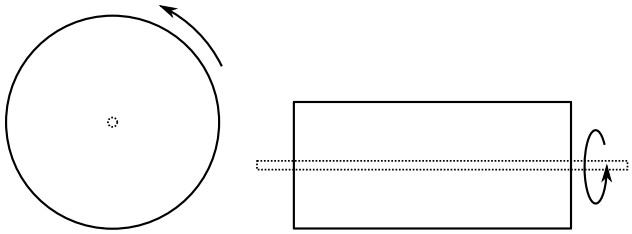

Figure 1.2: Equivalent cross-sectional areas for an AFT (left) and CFT (right) with the flow going into the figure plane demonstrates how CFTs can have a smaller transverse dimension due to their rectangular profile.

rotate on an axis that is perpendicular to the oncoming flow, and are now being explored for harvesting hydrokinetic as well as wind energy. The lift-based CFT is also known as a Darrieus turbine based on its inventor [5].

As demonstrated in figure 1.2, when operating in tidal flows or rivers, CFTs can extract energy from a larger cross-section of the flow in shallow currents as compared to an AFT by orienting horizontally, while maintaining lower blade tip speeds and hence posing less risk to aquatic life. In this configuration, multiple turbine units can be operated on the same axis of rotation as illustrated in figure 1.1b, driving a single generator, hence reducing the associated costs. The Ocean Renewable Power Company is successfully operating such cross-flow turbine prototypes in a tidal channel in Maine [4] and in a remote river in Alaska.

For harvesting wind energy, CFTs are installed vertically, also referred to as vertical axis wind turbines (VAWT), which allows the electrical equipment to be housed on the ground and provides ease of maintenance. CFTs when oriented vertically have the advantage of not requiring yaw control to align the axis of rotation with the horizontal flow like in AFTs. It has also been argued that they can provide a higher wind farm power density based on land use due to the rectangular cross-section mentioned above and constructive interference between the individual turbines [8].

An efficient design process for CFTs requires low-order models to predict their performance with a low computational cost. Such design tools are prevalent for AFTs since they have had a longer development period and are actively in production worldwide, however

(a) An "egg-beater" type CFT [6].

(b) A Gorlov type CFT that has helical blades [7].

(c) A straight-bladed CFT by Ropatec srl.

Figure 1.3: Different shapes of a cross-flow wind turbine.

they do not easily translate to CFT designs. Analytical techniques such as streamtube models [9] and vortex models [10, 11], or numerical models based on tabulated airfoil data [12, 13] have been implemented for CFTs. However low-order techniques which predict performance based on prior aerodynamic data for a non-rotating blade, even when collected under dynamic pitching/surging conditions similar to those experienced by a CFT blade, are not adequate. These do not account for detailed yet important flow phenomena such as the curvilinear nature of relative flow on the blade, the Coriolis force on the flow and the resulting vortex trapping at the blade [14], or the induced flow encountered on the downstream side including the blade-vortex interactions. Full Navier-Stokes simulations of a rotating CFT, that is, without using prior tabulated or time-averaged blade forces, provide high resolution data that can be used to identify the dominant flow features affecting turbine performance and hence aid in creating effective low-order models.

1.2 Operating principle

While curved or helical blades as seen in figures 1.1b, 1.3a, and 1.3b are also used for CFTs, this research is focused on a two-blade straight-bladed design. The straight-bladed

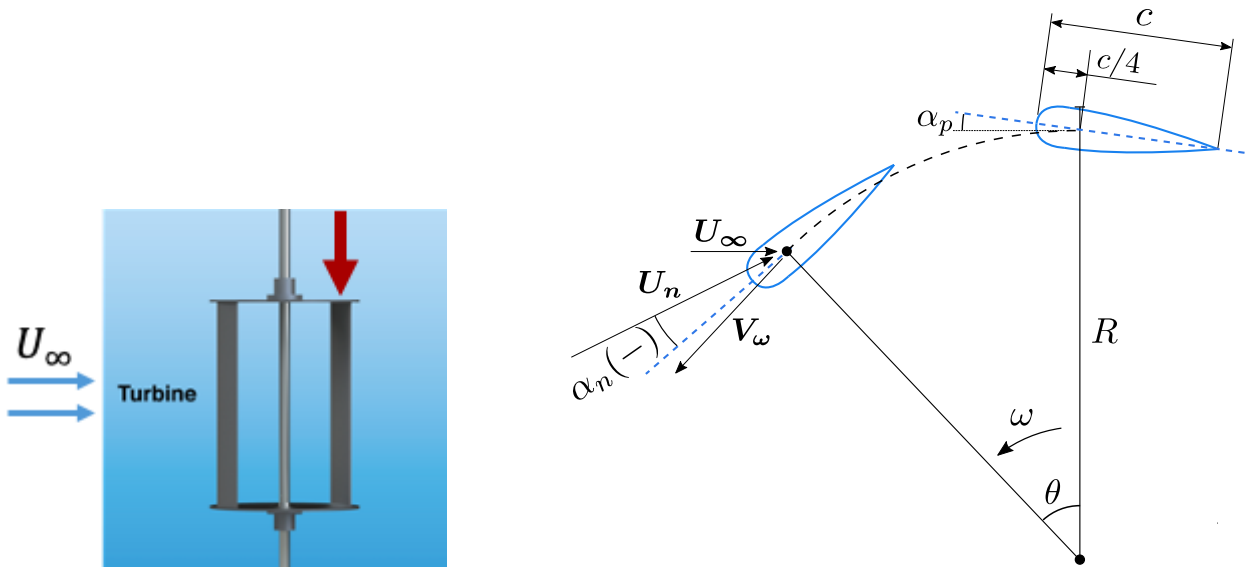

(a) A straight-bladed CFT.

(b) Nomenclature of turbine geometry and blade kinematics.

Figure 1.4: Schematic and nomenclature of a turbine blade cross-section as indicated by the red arrow in (a) is shown in (b).

design illustrated in figure 1.4a, also known as H-Darrieus, has benefits such as ease of manufacturing, and thus lower costs, and also ease of modeling. This particular turbine is designed for hydrokinetic energy extraction, and matches the experimental set-up at the Pacific Marine Energy Center at University of Washington. Figure 1.4b demonstrates the geometry and kinematics of a cross-flow turbine blade through a portion of its cycle. As the blade rotates in the freestream with an angular velocity, ω, the instantaneous velocity of the blade is shown as $\boldsymbol{V_\omega}$. Lift is generated through the apparent angle of attack, α_n, which is the angle the blade encounters with respect to the relative flow velocity, $\boldsymbol{U_n}$. The component of this lift force that is tangential to the blade motion drives the turbine. Turbine performance is characterized as a function of tip speed ratio, defined as the ratio of turbine tip speed to the flow freestream velocity,

$$\lambda(\theta) = \frac{\omega(\theta) R}{U_\infty}. \tag{1.1}$$

where R is the distance from center of the turbine to the outermost edge of the blade as shown in figure 1.4b. In this manuscript, $\theta = 0^\circ$ represents the foil position when the velocity vector of the foil is directly opposing the freestream velocity vector. Neglecting induced flow effects and the curvature of relative flow along blade chord, variation in α_n and U_n^* throughout the rotation of a blade is given by

$$\alpha_n(\theta) = -\tan^{-1}\left(\frac{\sin\theta}{\lambda(\theta)+\cos\theta}\right) + \alpha_p(\theta) \tag{1.2}$$

and

$$U_n^* = \frac{|\boldsymbol{U_n}(\theta)|}{U_\infty} = \sqrt{\lambda(\theta)^2 + 2\lambda(\theta)\cos\theta + 1}. \tag{1.3}$$

where the sign of α_n is positive when the relative flow velocity is directed outwards from the axis of rotation and negative when it is directed inwards as in figure 1.4b. The torque applied to the turbine by the fluid and the resultant power generated are normalized respectively as the torque coefficient and power coefficient,

$$C_Q(\theta) = \frac{q(\theta)}{\frac{1}{2}\rho U_\infty^2 A R} \tag{1.4}$$

and

$$C_P(\theta) = \frac{q(\theta)\omega(\theta)}{\frac{1}{2}\rho U_\infty^3 A}. \tag{1.5}$$

The power coefficient, C_P, is the conversion efficiency of the turbine defined by the ratio of the power generated to the power available in the projected area.

1.3 Turbine geometry and flow conditions

The turbine geometry in this computational investigation is designed to mimic a previous setup from experiments by Strom et al. [15] and Snortland et al. [16] with the exception that

it has no support structures such as the center drive shaft and the connecting struts. It is comprised of two NACA0018 foils with $c/R = 0.47$, mounted at the quarter chord location from the leading edge, and $\alpha_p = 6^\circ$ (leading edge angled outward). The Reynolds number based on blade chord length and freestream flow velocity is $Re = cU_\infty/\nu = 4.5 \times 10^4$. However, the local Re would depend on λ and varies throughout the rotation of the blade due to the variation in relative flow and flow induction.

As described above, some of the important non-dimensional parameters that govern the cross-flow turbine are its geometry (blade shape and pitch, number of blades, c/R), its kinematics (λ), and its configuration, or proximity to other surfaces such as walls, the free surface, or other turbines. The ratio of projected turbine area normal to the flow, A, to the total cross-sectional area of the flow is defined as the *blockage ratio*. It is well established that increasing the blockage ratio to an extent enhances power generation [17,18]. In the prior experiments [15,16], the turbine is oriented vertically, as shown in figure 1.4a, in a water channel that is enclosed by walls on three sides with a free surface on the top and a high blockage ratio of approximately 11%. While wind turbines are usually unconfined in actual deployment, hydrokinetic turbines may be placed in naturally confined flow, such as in shallow or narrow water channels. In this work, both a high blockage ratio of 10.6% (*confined configuration*) and zero or very low blockage (*unconfined configuration*) are simulated for a single turbine. This enables an analysis of the effect of confinement on the flow dynamics and consequently the turbine performance. Additionally, a turbine pair under very high confinement (up to 83%) is simulated as part of a co-design cycle estimating the cost of extracting energy from river or tidal channels using multiple turbines.

Within the scope of this work, only a two-dimensional or infinite-span blade is modeled. This prohibits exploring a three-dimensional confinement, and also the effects of the free surface or non-uniform velocity profiles [19,20], and thus the confinement estimates do not precisely match experiments. Another parameter of interest in turbine design is the aspect ratio, that is, the ratio of turbine span to diameter. This has been found to not affect

the efficiency of a CFT with other non-dimensional parameters held constant [21], and its effect cannot been examined in this work as the full blade span is not modeled.

1.4 Dynamic stall on blades

Figure 1.5 shows the variation of α_n and U_n^* during a rotation cycle for two tip speed ratios, computed with equations 1.2 and 1.3. Torque generation on a single blade (from a two-bladed turbine), obtained through large-eddy simulation (LES), is also included as an example. The apparent angle of attack undergoes very high variation during the cycle, reaching -25° to $+35^\circ$ for $\lambda = 1.9$ and approximately +/- 60° for $\lambda = 1.1$, which is much higher than the critical angle of attack for flow separation on a stationary foil ($\approx 12^\circ$) [22]. Although the computed angle of attack in figure 1.5 does not account for the effect of induction, the high variation creates flow transitions from attached flow to highly separated flow and vice versa, a phenomenon known as dynamic stall.

This is observed in the vorticity field in figure 1.5 from LES at $\lambda = 1.9$. While the flow is attached at the inward side of the upstream blade at $\theta = 64^\circ$, a significant separation can be seen at $\theta = 129^\circ$. The flow reattaches to the blade at the end of its upstream motion as the angle of attack switches signs and the outward side of the blade becomes prone to separation during the downstream motion. Uncontrolled dynamic stall produces a drop in the lift-to-drag ratio, decreasing the torque generated. For the turbine shown in figure 1.5, the torque for $\lambda = 1.9$ starts to peak at $\theta = 90^\circ$ due to the dynamic stall on the blade along with the decreasing U_n^*. Although not shown in figure 1.5, these dynamic stall events can cause undesirable load oscillations, which contribute to fatigue or structural failure and makes self-starting difficult [23, 24], especially at low Reynolds number.

Due to the challenges posed by dynamic stall in CFTs, it has been studied through laboratory experiments such as in [25] where generation of two pairs of stall vortices at the blade has been observed during rotation, and in [26] where the circulation of the leading

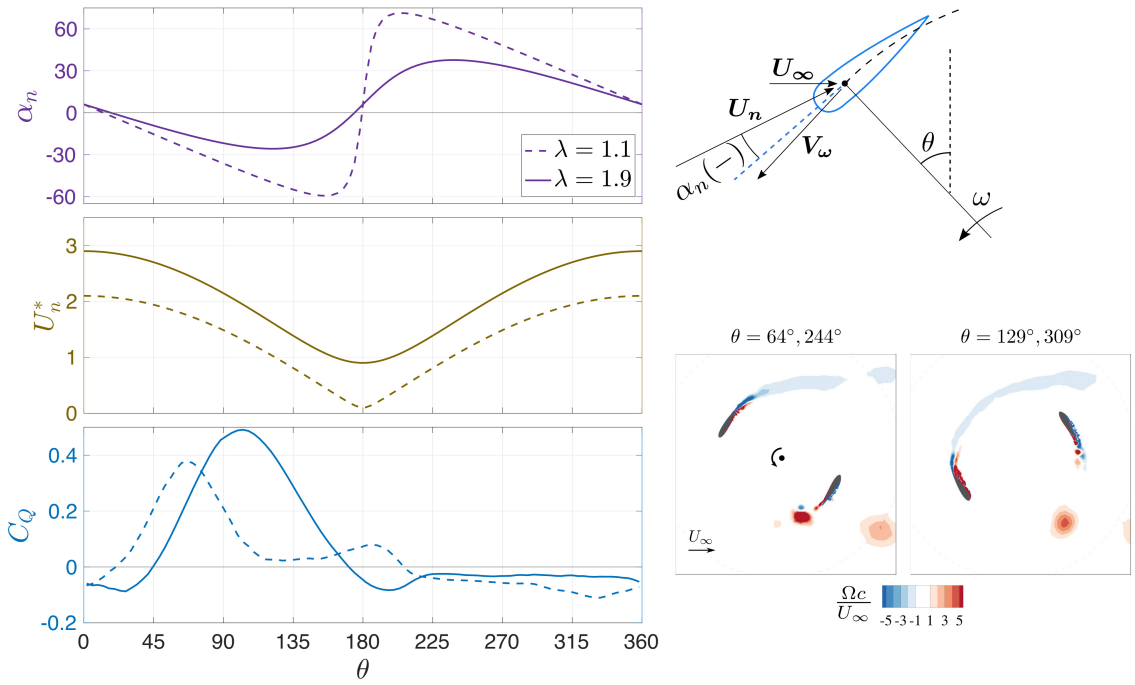

Figure 1.5: The top two frames show the variation of relative flow on the blade for a full rotation, computed with equations 1.2 and 1.3. The bottom frame shows the torque coefficient for a single blade from LES of a two-blade turbine. Vorticity fields demonstrate flow separation on the upstream blade from LES of a two-blade turbine with $\lambda = 1.9$.

edge vortex (LEV) is analyzed along with the roll up and formation of a trailing edge vortex (TEV). Using computations in [14], the Coriolis effect has been shown to result in the turbine blade capturing a vortex pair at low tip speed ratios after the angle of attack starts decreasing. This negatively affects torque generation and cannot be reproduced by a non-rotational pitching-surging blade with an equivalent angle of attack and relative velocity variation. Wang et al. also observed how vortex dynamics plays a role in reduction of power conversion at both low and high tip speed ratios [27].

Due to these non-linear vortex dynamics and blade-vortex interactions in CFTs, a generic dynamic stall model based on blade forces for similar pitching/surging rates is not adequate to predict turbine performance, much less the flow field around and in the wake of the turbine. While experiments are used for collecting performance data and flow visualization, exploring multiple geometric configurations of a turbine can be a tedious process, and it is

challenging to visualize the flow field near to the blades at an adequate resolution. Hence experiments need to be complemented with CFD to understand the basic flow dynamics and obtain highly resolved flow field data to create lower order design tools for CFTs. Turbulence modeling in computations involving dynamic stall pose a challenge of their own, which is explored throughout this thesis.

1.5 Research goals and thesis outline

Computational methods (chapter 2)

The turbulence model, mesh, and validation with experiments are presented for the unsteady Reynolds-averaged Navier-Stokes (RANS) and large-eddy simulations (LES).

Comparison of LES with RANS under varying confinement (chapter 3)

Whereas RANS computations have the advantage of a quick turn-around time in providing an estimate of turbine performance, especially for a two-dimensional simulation, they are unable to accurately predict characteristics of dynamic stall in some instances. Hence higher fidelity large-eddy simulations (LES) are often performed for accurately simulating the occurrence of stall, the resulting vortex dynamics and flow field in the wake. Past literature when comparing RANS and LES modeling for a CFT, has not examined the effect of confinement. Thus wall-resolved LES of the current CFT is performed, particularly investigating the interaction of confinement with the modeling technique, and evaluating the strengths and limitations of 2D RANS in modeling the dynamic stall process and the turbine wake.

This work also contributes to a multi-disciplinary project investigating the reduction of levelized cost of energy (LCOE) for CFTs to 0.1$/kWh by using multiple turbines to increase the overall confinement in river or tidal channels. A turbine pair with cumulative

blockage up to 83% is simulated as part of the co-design cycle using the RANS model, while comparing with LES at specific parameters to verify the accuracy of the flow physics.

Analysis of dynamic stall development using modal decomposition (chapter 4)

For an efficient design process for CFTs, low-order models are required, which can predict their performance while considering the complex dynamic stall phenomenon, the resulting flow structures, and interactions with the blades. Theoretical models or numerical ones based on tabulated aerodynamic forces for the blade are not able to account for these non-linear effects. Modal decomposition of flow fields has been previously used to dissect the dynamic stall [28, 29], but seldom for a rotating blade. Based on high resolution flow field data obtained from LES, the dominant flow features at the blade through its rotation are identified through proper orthogonal decomposition. Their time evolution is correlated with the blade aerodynamic loads and critical events in the stall cycle, with potential application to separation control.

Intracycle control of angular velocity (chapter 5)

The dynamic stall behavior of a CFT can be altered by modifying the α_n and U_n^* profiles experienced by the blade. One method of effecting this change is the variation of ω, and hence λ, throughout the rotation of a CFT rather than keeping it constant. Such an *intracycle* variation of ω, when optimized in a previous experiment, increased the mean power coefficient of a CFT in confined flow by up to 57% [15]. However, no flow visualization was performed to determine the mechanisms causing this enhancement while it is hypothesized that the nonlinear dynamic stall process was impacted. LES is performed to investigate this by visualizing the changes in flow at the blade while extracting a common basis of modes with the constant rotation simulation and hence directly comparing the spatio-temporal flow evolution.

1.6 Research products

Completed and anticipated journal articles

1. *Dave, M., Spaulding, A., & Franck, J. A. (2020). Variable thrust and high efficiency propulsion with oscillating foils at high Reynolds numbers. Ocean Engineering, 214, 107833. https://doi.org/10.1016/j.oceaneng.2020.107833*

   The article is not represented in this thesis. RANS computations are performed for a heaving-pitching foil with a large heave amplitude and at a fully turbulent Re. Results illustrate the kinematics required to transition between the high-efficiency and high-thrust regimes and are classified into flow regimes based on performance and vortex structure in the wake.

2. *Calvet, A. G., Dave, M., & Franck, J. A. (2021). Unsupervised clustering and performance prediction of vortex wakes from bio-inspired propulsors. Bioinspiration & Biomimetics, 16, 046015. https://doi.org/10.1088/1748-3190/ac011f*

   The article is not represented in this thesis. An unsupervised machine learning strategy is developed to automatically cluster the wakes of bio-inspired propulsors into groups of similar propulsive thrust and efficiency metrics based on vorticity images from CFD simulations. Contribution: performing RANS computations and preparing the manuscript.

3. *Dave, M., Strom, B., Snortland, A., Williams, O., Polagye, B., & Franck, J. A. (2021). Simulations of intracycle angular velocity control for a crossflow turbine. AIAA Journal, 59(3), 812824. https://doi.org/10.2514/1.J059797*

   The article is partly represented in chapter 2.

4. *Dave, M., & Franck, J. A. (2021). Comparison of RANS and LES for a cross-flow turbine in confined and unconfined flow. Journal of Renewable and Sustainable Energy, 13(6), 064503. https://doi.org/10.1063/5.0066392*

The article is presented here as chapter 3.

5. *Dave, M., & Franck, J. A. (2021). Development and control of dynamic stall on a cross-flow turbine blade.*

   The manuscript is under preparation for submission to the Physical Review Fluids journal, and is presented in this thesis as chapters 4 and 5.

Conference and invited presentations

1. Dave, M., Spaulding, A., & Franck, J. A. (Nov 2018). RANS Simulations of Oscillating Foils for High-Thrust Marine Propulsion. APS Division of Fluid Dynamics, Atlanta, GA.

2. Dave, M., Calvet, A. G., & Franck, J. A. (Nov 2019). Clustering of Vortex Wakes for Heaving-Pitching Foils Using Machine Learning. APS Division of Fluid Dynamics, Seattle, WA.

3. Dave, M., Strom, B., & Franck, J. A. (Jan 2020). Vortex Dynamics of Darrieus Turbines with Intracycle Angular Velocity Control. AIAA Scitech Forum, Orlando, FL.

4. Dave, M., Strom, B., Snortland, A., Williams, O., Polagye, B., & Franck, J. A. (Sep 2020). Simulations of Intracycle Angular Velocity Control for a Cross-Flow Turbine. Pacific Marine Energy Center (PMEC) All-Center Meeting (virtual).

5. Dave, M., & Franck, J. A. (Nov 2020). Large-eddy Simulations of a Cross-Flow Turbine. APS Division of Fluid Dynamics (virtual).

6. Dave, M., & Franck, J. A. (Mar 2021). Computations of Dynamic Stall in a Cross-Flow Turbine. Fluid Talks webinar series by the Fluids Early Career Researcher Forum (virtual), Leeds Institute for Fluid Dynamics, University of Leeds, United Kingdom.

7. Dave, M. (Jul 2021). Simulations of Unsteady Flow Phenomena in a Cross-Flow Turbine. Department Student Research Committee seminar (virtual), Indian Institute of Science, Bengaluru, India.

8. Dave, M. (Jul 2021). Simulations of Dynamic Stall in Cross-Flow Turbines. Sabarmati Young Researcher Seminar (virtual), Indian Institute of Technology, Gandhinagar, India.

9. Dave, M., & Franck, J. A. (Aug 2021). Investigation of Dynamic Stall within a Cross-Flow Turbine via Large-eddy Simulation. AIAA Aviation Forum (virtual).

10. Dave, M., & Franck, J. A. (Nov 2021). Modal Analysis of Dynamic Stall on a Cross-Flow Turbine Blade . APS Division of Fluid Dynamics, Phoenix, AZ.

11. Dave, M., & Franck, J. A. (May 2022). Dominant Flow Features on a Cross-Flow Turbine Blade with Constant and Intracycle Angular Velocity. Direct In-person Colloquium on Vortex Dominated Flows (DisCoVor), Villars-sur-Ollon, Switzerland.

12. Dave, M., & Franck, J. A. (Nov 2022). Investigation of Dynamic Stall on a Cross-Flow Turbine Blade using Modal Decomposition. APS Division of Fluid Dynamics, Indianapolis, IN.

2 Computational methods

2.1 Reynolds-averaged Navier Stokes (RANS) simulation

Numerical model

The governing equations for the incompressible unsteady RANS computations are

$$\nabla \cdot \overline{\boldsymbol{u}} = 0 \tag{2.1}$$

$$\frac{\partial \overline{\boldsymbol{u}}}{\partial t} + (\overline{\boldsymbol{u}} \cdot \nabla)\overline{\boldsymbol{u}} = -\nabla \overline{p} + \nu \nabla^2 \overline{\boldsymbol{u}} - \nabla \cdot \boldsymbol{\tau}. \tag{2.2}$$

These equations are solved using a second-order accurate finite volume, pressure-implicit split-operator (PISO) method [30] implemented in *OpenFOAM* [31]. The Reynolds stress tensor, $\boldsymbol{\tau}$, in equation 2.2 is modeled with the k-ω SST equations [32]. The k-ω SST model has been used extensively in RANS simulations of cross-flow turbines [33–39] and is found to be a desirable closure model due to its documented ability of handling separated flows [40]. It was able to predict the C_P vs λ curve most accurately as compared to other RANS models when validated with multiple experiments and factoring in corrections for losses from the support structure [41].

Computational domain and boundary conditions

The simulation domain contains an inner mesh of radius $4c$ with a sliding interface between this rotating inner region and the intermediate wake-region mesh that remains stationary (figure 2.1). The wake region extends $27c$ downstream of the turbine center, while the outermost region of the domain extends $250c$ downstream and $200c$ upstream of the turbine center. For the confined configuration, the domain width along y-direction is $40c$,

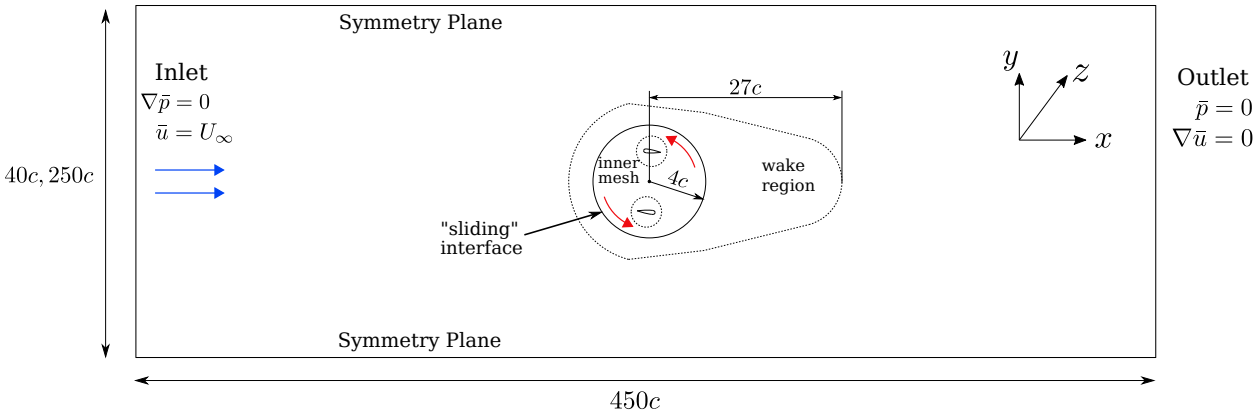

Figure 2.1: Schematic representation of the computational domain.

and the resulting blockage is 10.6%. The performance is also tested with an unconfined configuration that has a width of $250c$ corresponding to a blockage ratio of 1.7%. A constant inlet flow velocity along x is prescribed on the left boundary while a constant pressure value is prescribed at the outlet boundary. A symmetry boundary condition is prescribed at the top and bottom that enforces zero normal flow velocity through the boundaries. A zero-gradient boundary condition is applied to the turbulent kinetic energy at the foil. A wall function is utilized to calculate the specific dissipation for the first layer of mesh cells at the foil, that implements a blending function of its viscous sub-layer and log-law region variations based on distance from the wall [42].

For conditions where the flow separates from the blade, such as for the unconfined configuration, the results are particularly sensitive to the prescribed value of the far-field turbulent kinetic energy, k, which is used as a tuning parameter when benchmarking against experimental results. There is no data readily available for unconfined configurations of this particular turbine. Barnsley and Wellicome's blockage correction [43] has been found to yield good predictions of power generation in unconfined flow from experimental results for confined flow [18]. This correction is applied to the experimental data, and prescribing a far-field value of $k = 1 \times 10^{-5}$ yields a power coefficient within 6.6% of the predicted blockage-corrected value for $\lambda = 1.9$.

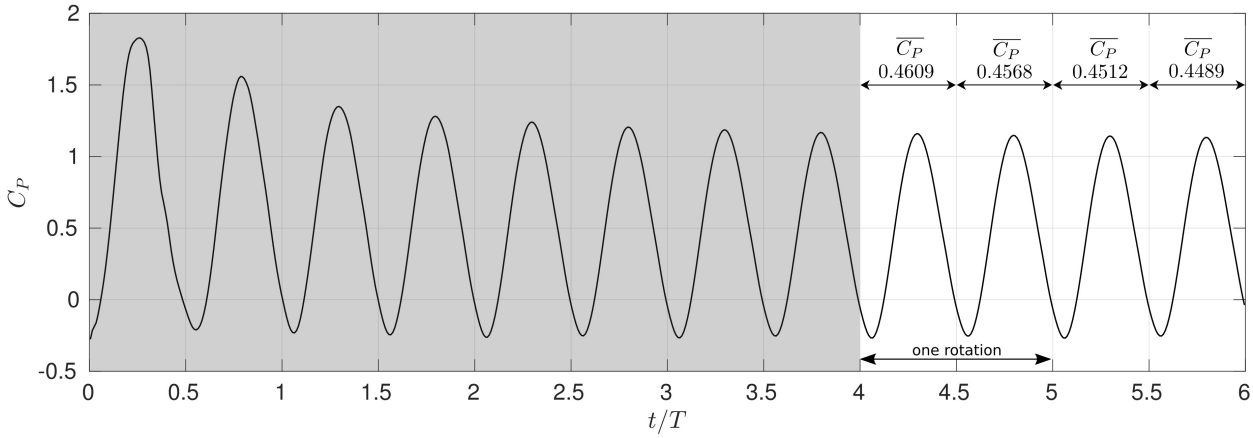

Figure 2.2: Evolution of C_P over six rotations and twelve phase cycles from RANS computations with confined flow at $\lambda = 1.9$. The grey background indicates the developing flow state, and the white background indicates developed flow or steady state over which the power coefficient is averaged.

Mesh sensitivity and validation

Simulations with a constant ω corresponding to $\lambda = 1.9$ are performed for the mesh-sensitivity analysis. Figure 1.5 shows the variation of α_n and U_n^* during a rotation cycle. Before rotation, a fully-developed state is achieved by running the simulation with stationary blades. The rotating simulation is then run for six blade revolutions. Figure 2.2 shows the variation of power coefficient for the confined flow within these six complete revolutions. The force and moment values are phase-averaged over the last four half-revolutions to get the mean values once a fully developed state is reached (one phase cycle equals a half-revolution due to the symmetry of a two-blade turbine).

Simulations are performed with various mesh configurations and the results are directly compared with experimental data to determine an appropriate computational setup. Results for six mesh configurations are presented in table 2.1. Mesh A is shown at different levels of resolution in figure 2.3. The boundary layer region around the foil is resolved with layers of body-fitted structured mesh elements (figure 2.3d) which transition to unstructured elements with gradually decreasing levels of refinement. For all mesh configurations, the number of mesh points along the foil boundary is 523, the wall-normal distance of the

		$\Delta y/c$ for first mesh layer	No. of body-fitted layers	No. of cells in the inner mesh	Total no. of cells	Reynolds number	$\overline{C_P}$
confined	mesh A	0.001	60	178,077	272,892	4.5×10^4	0.454
	mesh B	0.001	60	318,837	400,646	4.5×10^4	0.437
	mesh C	0.0005	60	316,017	420,352	4.5×10^4	0.441
	Experimental data					4.5×10^4	0.377
unconfined	mesh D	0.001	60	223,357	307,300	4.5×10^4	0.228
	mesh E	0.001	60	318,837	427,870	4.5×10^4	0.324
	mesh E					1×10^5	0.430
	mesh F	0.001	60	370,409	535,720	4.5×10^4	0.346
	Experimental data with blockage correction					4.5×10^4	0.305

Table 2.1: Details of different mesh configurations demonstrating mesh sensitivity for the RANS simulations. The highlighted meshes are selected for the simulations. ($\lambda = 1.9,\ Re = 4.5\times10^4$)

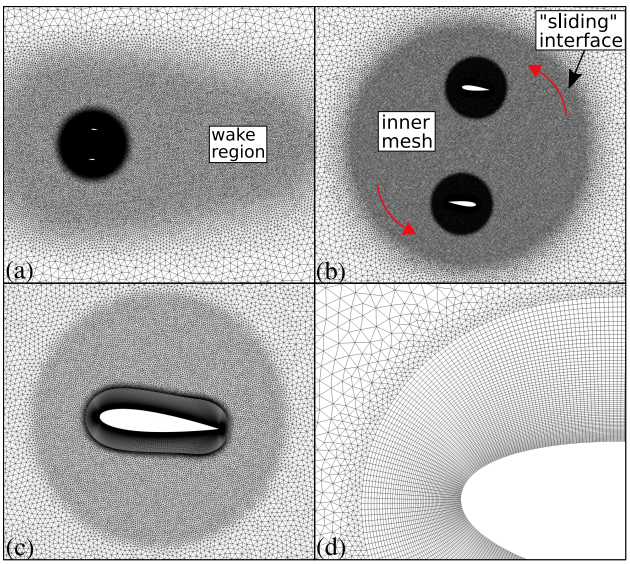

Figure 2.3: Layers of computational mesh with increasing level of resolution: (a) Immediate surrounding of the inner mesh (wake region). (b) Rotating inner mesh. (c) Mesh around the foil. (d) Body-fitted structured mesh to resolve the boundary layer.

first mesh layer, $\Delta y/c$, is given in table 2.1, and the mesh points within the boundary layer increase by a growth factor ≤ 1.1.

Table 2.1 tabulates the mean power coefficient for each of these meshes over the last four phase periods. The power coefficient and normalized forces vary minimally between the

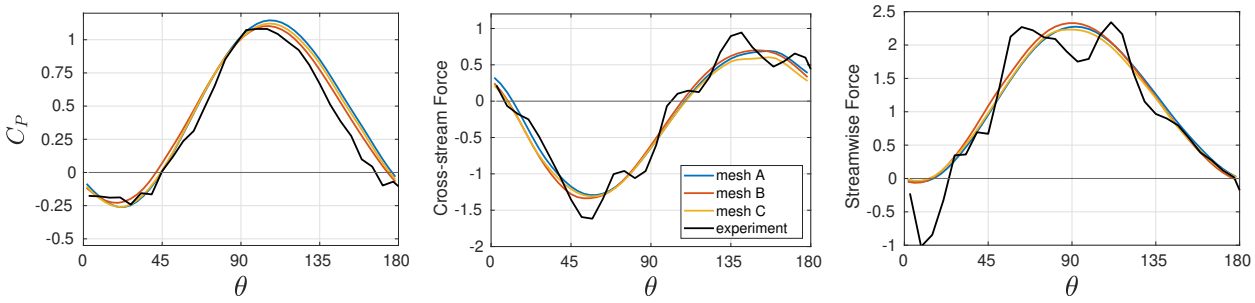

Figure 2.4: Power coefficient and force coefficients from RANS simulations for three different mesh configurations for confined flow (blockage ratio = 10.6%), and from experimental data (blockage ratio = 11.6%) for $\lambda = 1.9,\ Re = 4.5 \times 10^4$. Mesh A is selected for the final analysis with confined flow.

meshes A, B, and C, hence mesh A is chosen for performing the confined flow simulations. Mesh E is chosen for the unconfined simulations as the power and forces computed don't vary significantly between mesh E and mesh F. For mesh A and mesh E, the maximum value of y^+ for the first mesh layer at the foil, for a stationary foil with 6° angle of attack is 1.76 and 1.61 respectively.

The computed power coefficient and force coefficients for the confined flow are shown in figure 2.4 and directly compared with experiments by Snortland et al. [16], which are conducted at similar blockage ratio and Reynolds number to the computations. Streamwise and cross-stream forces are not reported in [16], but acquired simultaneously by the 6-axis load cells mounted at either end of the turbine rotor and included here to augment validation. As the simulations do not include support structures, the torques and forces on the blades were estimated from the experimental data by subtracting the torques and forces arising from rotating only the center shaft and struts at the same inflow velocity from those for the full turbine. The confined flow simulations show good agreement with experiments while over-predicting the peak power coefficient. There are fluctuations present in the experimentally measured forces which are likely associated with mechanical and hydrodynamic resonance of the experimental setup, however the values about which they fluctuate match with the computations.

Results are also compared to experiments at a lower tip speed ratio. At $\lambda = 1.1$, the

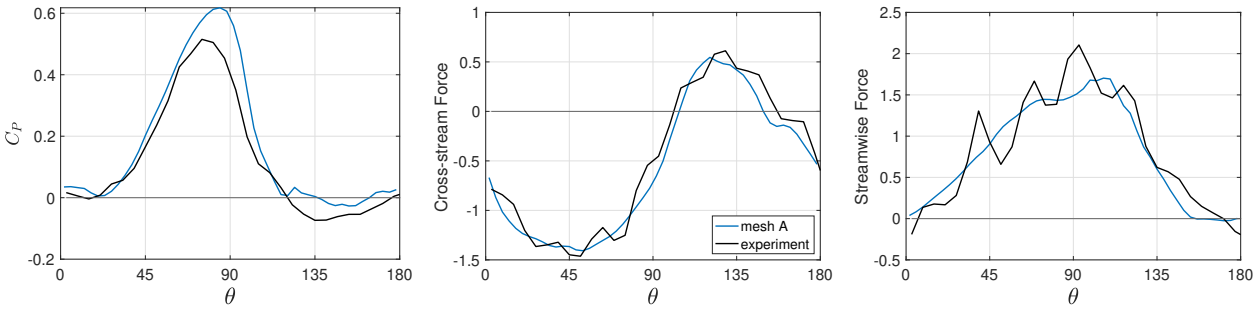

(a) Power coefficient and force coefficients from RANS simulations (blockage ratio = 10.6%), and from experimental data (blockage ratio = 11.6%) for $\lambda = 1.1,\ Re = 4.5 \times 10^4$.

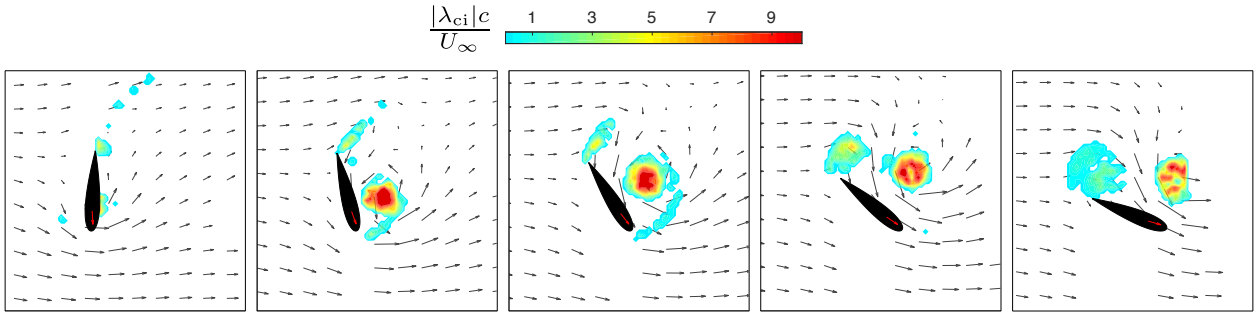

(b) Experimental data - PIV, blockage ratio = 11.6%

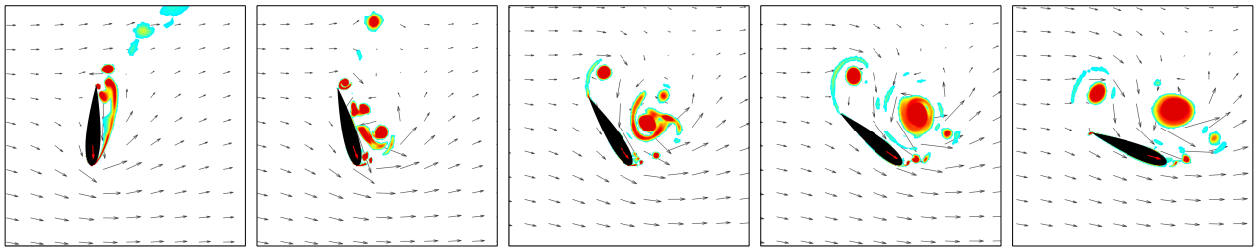

(c) RANS simulations, blockage ratio = 10.6%

Figure 2.5: (b)(c) Instantaneous flow velocity (vectors) and swirl strength (contours) from experimental data and RANS simulations show the generation of an LEV between $\theta = 90°$ to $\theta = 180°$ for $\lambda = 1.1,\ Re = 4.5 \times 10^4$.

blades experience higher angles of attack as seen in figure 1.5, and hence experience a deeper dynamic stall with separated flow over majority of the upstream sweep of the blade, which results in poor power generation. Figure 2.5a compares the torque and forces for the confined flow computations with the experiments by Snortland et al. [16]. The peak power is over-predicted, along with discrepancies between $\theta = 120°$ to $\theta = 180°$. Figures 2.5b and

2.5c directly compare the velocity and swirl strength from the computations with the phase-averaged particle image velocimetry (PIV) data from the experiments. The swirl strength is obtained by an eigenvalue analysis of the velocity gradient tensor [44, 45]. It denotes the amount of local swirling motion of the flow and hence can be used to differentiate vortices from shear layers. The flow field shows the generation of an LEV between $\theta = 90^\circ$ to $\theta = 180^\circ$ due to flow separation on the upstream foil. The apparent angle of attack increases to its maximum value and then rapidly drops to zero during this part of the rotation (figure 1.5) which generates an LEV that is shed from the foil. This process corresponds to a drop in torque generation. The computed and experimental flow fields match well in terms of location and strength of the LEV, and the surrounding velocity field.

The discrepancy in C_P observed at $\lambda = 1.1$ may be due to the difficulty of simulating highly separated flow using a RANS model. The two-dimensional approximation of the flow field cannot capture the three-dimensional instabilities inherent to high Reynolds number flows, including those within the boundary layer that affect transition and flow separation phenomena. Results also indicate high sensitivity to the Reynolds number in the regime explored, especially for the unconfined flow. The intrinsic transitional nature of the flow physics, and the varying of relative flow velocity throughout the cycle make this regime computationally challenging. Increasing Re from 4.5×10^4 to 1×10^5 for the unconfined configuration at $\lambda = 1.9$ increases the mean C_P from 0.324 to 0.430, as shown in table 2.1. Due to the experimental conditions, the moderate Reynolds number of 4.5×10^4 remains the focus of this study.

2.2 Large-eddy simulation (LES)

Numerical model

LES solves the spatially filtered incompressible Navier-Stokes equations,

$$\frac{\partial \tilde{u}_i}{\partial x_i} = 0 \tag{2.3}$$

and

$$\frac{\partial \tilde{u}_j}{\partial t} + \frac{\partial \tilde{u}_i \tilde{u}_j}{\partial x_i} = -\frac{1}{\rho}\frac{\partial \tilde{p}}{\partial x_j} + \nu \frac{\partial^2 \tilde{u}_j}{\partial x_i \partial x_i} - \frac{\partial \tau_{ij}}{\partial x_i}, \tag{2.4}$$

where τ_{ij} represents the sub-grid scale (SGS) stress tensor,

$$\tau_{ij} = \widetilde{u_i u_j} - \tilde{u}_i \tilde{u}_j. \tag{2.5}$$

For the local dynamic k-equation SGS model [46], τ_{ij} is modeled as,

$$\tau_{ij} = -2C_k \Delta \sqrt{k}\, \tilde{S_{ij}} + \frac{2}{3}\delta_{ij} k \tag{2.6}$$

where $\tilde{S_{ij}}$ represents the filtered rate of strain,

$$\tilde{S_{ij}} = \frac{1}{2}\left(\frac{\partial \tilde{u}_i}{\partial x_j} + \frac{\partial \tilde{u}_j}{\partial x_i}\right). \tag{2.7}$$

In equation 2.6, Δ is a measure of the size of the mesh cell, computed as cube-root of the cell volume, that acts as the implicit filter size. A smoothing restriction is also imposed which prevents large changes in Δ between neighboring mesh cells. The SGS kinetic energy, k, is computed by its transport equation. The coefficient C_k in equation 2.6 and a coefficient of dissipation in the transport equation of k are computed dynamically from local flow properties utilizing the concept of similarity at two different length scales, that is, when a larger test filter is applied over an already filtered flow field, the SGS stress and the

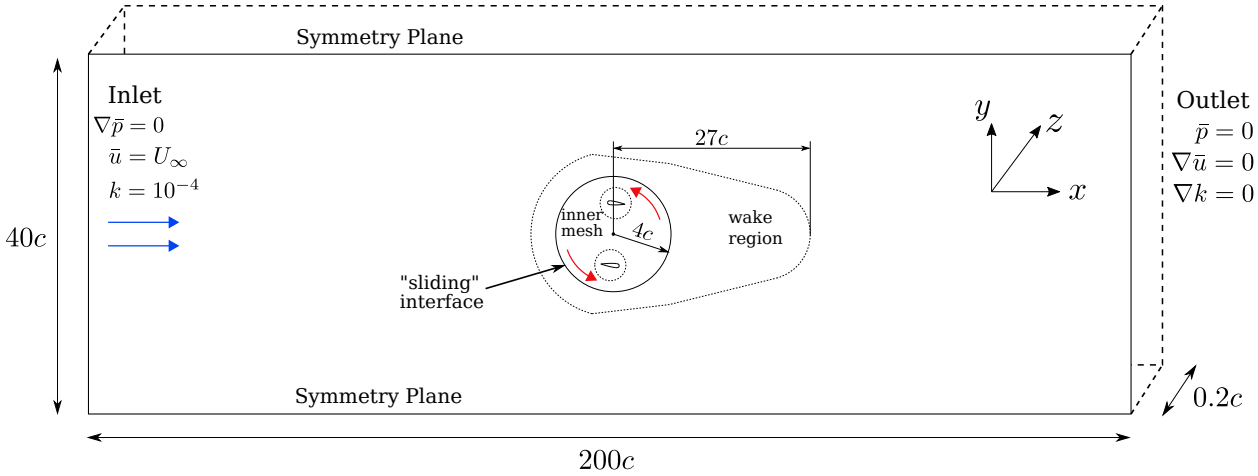

Figure 2.6: Schematic representation of the confined computational domain.

dissipation of k at the two different filter levels are similar [46]. The filtered Navier-Stokes equations along with the transport equation for k are solved using a second-order accurate finite volume solver from the *OpenFOAM* package [31].

Computational domain and boundary conditions

A representation of the computational domain for the turbine simulations is shown in figure 2.6. An inner mesh region, that includes the two blades of the turbine, rotates while the surrounding mesh remains stationary, with a sliding interface between the two. Support structure such as the center rod and the connecting struts are not simulated. The freestream flow is along x-direction with inlet boundary conditions specified at the left boundary and outflow conditions at the right boundary. Only a small span of the blades $(0.2c)$ along the z-direction is simulated with periodic boundary conditions between the front and back planes. Two different configurations are investigated in terms of the blockage across the y-direction. The first is a *confined* configuration that has a domain width of $40c$ along y-direction with no flow being allowed to cross the top and bottom walls, resulting in a high blockage ratio of 10.6%. The second is an *unconfined* configuration that has a domain width of $200c$ along y-direction with outflow conditions at the top and bottom boundaries, allowing for a flow unconfined by walls. SGS kinetic energy for the incoming flow is

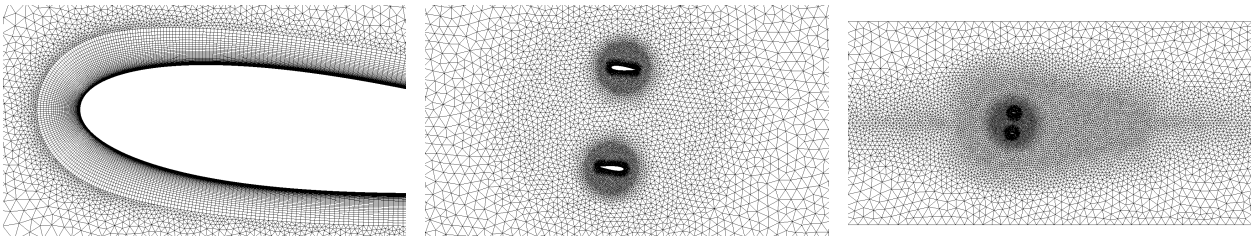

Figure 2.7: Snapshots of the mesh (confined), zooming out from left to right.

prescribed as $k/U_\infty^2 = 1 \times 10^{-4}$, while it was observed that the results were not sensitive to changes in this value due to the energy dissipation between the inlet and the turbine. At the blade, a zero normal gradient is imposed for $\tilde{p}$ and k.

Mesh and model sensitivity

The mesh for the confined configuration in the x-y plane is shown in figure 2.7. At each blade, 50 layers of quadrilateral mesh cells are used for resolving the boundary layer such that the maximum dimensionless wall distance, y^+, at the first mesh layer is less than 1. The structured mesh layers transition to an unstructured mesh that becomes coarser, with an intermediate relatively refined wake region between the far-field mesh and the inner rotating region. A single x-y mesh plane is extruded along the blade span of $0.2c$ in the z-direction to construct 48 mesh planes.

Six rotations of the turbine are simulated and the last two rotations are considered for analysis since the power generation stops changing significantly from one rotation to another. For a two-blade turbine, a repeated cycle of total power generation from both blades spans $180°$, a half rotation. Forces on the blades, the power generated, and often the flow variables are averaged over the four phase cycles to remove cycle-to-cycle variations, which is referred to as a “phase-averaged" quantity in this manuscript. However forces and power presented for a single blade are averaged over two of their individual phase cycles spanning $360°$ and also averaged over the two blades.

To assess the sensitivity of the mesh resolution and the SGS turbulence model, figure 2.8 compares the phase-averaged power coefficients for three different confined mesh

Mesh	No. of cells in each x-y plane	No. of mesh planes along span (z)	Total no. of cells	SGS models tested
1	94,566	48	4.54M	dyn-k, const-k, Smag, WALE
2	94,566	32	3.03M	dyn-k
3	86,886	48	4.17M	dyn-k

Table 2.2: Details of the mesh and models tested for a sensitivity analysis.

configurations as listed in table 2.2 for a tip speed ratio of $\lambda = 1.9$. Four different SGS models are tested for mesh 1 - the local dynamic k-equation model [46] (dyn-k), the constant coefficient k-equation model [47] (const-k), the constant coefficient Smagorinsky model [48] (Smag), and the wall-adapted local eddy-viscosity model [49] (WALE). The model coefficients for the latter three models have to be specified as they are not computed dynamically. The van Driest function [50] is used for the const-k and Smag models to damp the value of eddy-viscosity at the wall. Experimental data with a blockage ratio of 11.6% [16] is included for validation. The excellent agreement in figure 2.8 between the three mesh configurations with the dynamic coefficient k-equation model implies that mesh 1 is adequately well resolved and robust to small changes in the mesh.

Simulations for flow past a cylinder implemented in *OpenFOAM* have shown the local dynamic k-equation model to be the closest to experiments among the four models explored here [51,52]. Owing to this, and the closeness to previous experiment in figure 2.8, it is the chosen SGS model for this research. The constant coefficient k-equation and Smagorinsky models deviate drastically from the dynamic k-equation model. Designed for isotropic turbulence, they are known to over-predict dissipation [53], hence resisting the transition to turbulence at a wall and not able to accurately model separating flow at a moderate Re. However the wall-adapted LES model which is a constant coefficient model based on the square of the velocity gradient tensor, in contrast to the other three models that are based on the rate of strain tensor, overcomes the above-mentioned limitation near walls and exactly matches the dyn-k model predictions.

Figure 2.9 shows the instantaneous span-averaged vorticity fields around the blades.

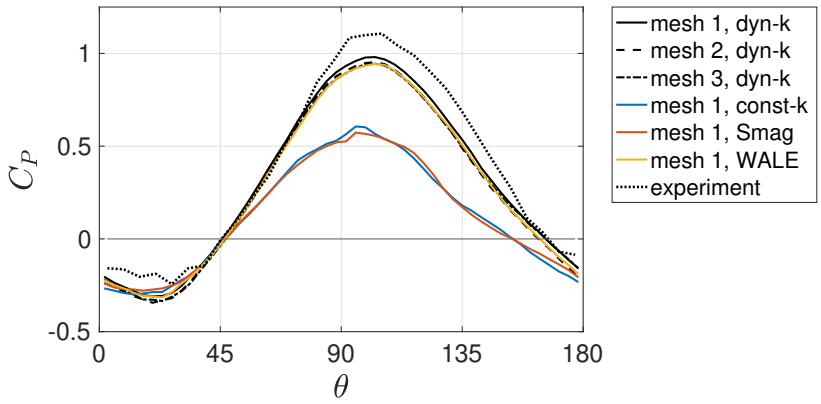

Figure 2.8: Power coefficient for the different mesh and model configurations. Blockage ratio = 10.6%, $\lambda = 1.9,\ Re = 4.5 \times 10^4$.

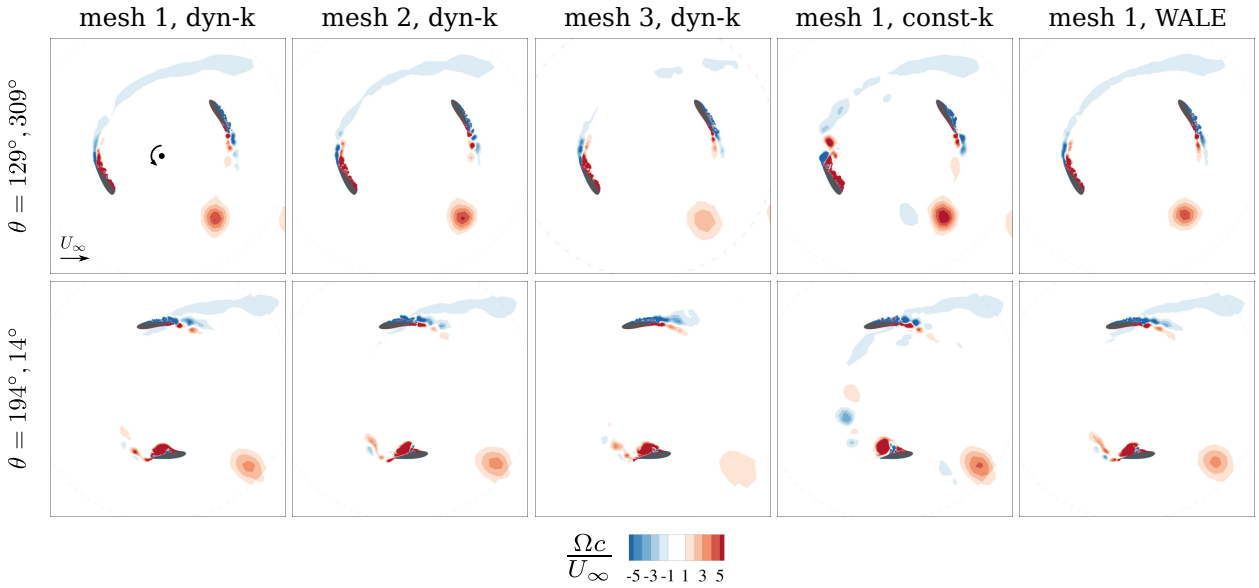

Figure 2.9: Normalized span-averaged vorticity fields for the different meshes and models. Blockage ratio = 10.6%, $\lambda = 1.9,\ Re = 4.5 \times 10^4$.

There are small differences between mesh 1, 2, and 3 in the formation and shedding of the LEV. Mesh 3 also results in a faster dissipation of the shed LEV presumably due to numerical dissipation from the coarser mesh. The constant coefficient k-equation model shows a larger flow separation due to its tendency to over-predict dissipation as mentioned above hence explaining the lower power generation observed in figure 2.8. The vorticity field for the Smagorinsky model, not shown here, is also qualitatively similar to the const-k model. The vorticity for the WALE model matches quite well to the dyn-k model and hence

it seems to successfully overcome the limitations of the Smag and const-k models in terms of the qualitative nature of the flow too.

3 Comparison of LES with RANS under varying confinement

3.1 Literature review: RANS and LES modeling of cross-flow turbines

Many researchers, including the current authors, have utilized two-dimensional unsteady Reynolds-averaged Navier-Stokes (RANS) models to efficiently model the performance and dynamics within each stroke [33,34,36,39,41,54–56]. Although many have compared favorably with experiments, there is evidence that the dynamic stall process may not be accurately captured [57–59]. Three-dimensional RANS has also been performed with modest success [33, 60–63] but still suffers from inaccurate time evolution of unsteady phenomena. As an example, when RANS computations are compared to large-eddy simulations (LES) it is shown that the RANS delayed the occurrence of dynamic stall compared to the LES [64,65], and results from LES are more comparable to the wind tunnel data in terms of forces and power generation.

Similarly, fully 3D LES [65] or hybrid RANS-LES models [66,67] that include the full span of the turbine blades also show better match with experiments and more realistic vortex formations as compared to fully 3D RANS. In Ref. [68], LES has been able to accurately predict the mean performance curve of a CFT as a function of its tip speed ratio when validated with experiments, and is further utilized to analyze the complex blade-vortex interactions.

Although it has been shown as an accurate modeling tool for the dynamic separation and reattachment on the blade, LES requires a three-dimensional computational domain for a physically consistent solution of the governing equations. In addition, it demands

high mesh resolution at the blade when fully resolving the boundary layer without the use of wall functions, known as wall-resolved LES or WRLES, hence significantly driving up the computational cost.

Another challenge in computational models of CFTs is the prediction of array interactions among individual turbines which requires accurate resolution of the unsteady flow physics and vortex dynamics. Velocity fields in the wake of a CFT have been examined in multiple experiments, along with the role of vortex structures from dynamic stall in re-energizing the wake. In Ref. [69], the wake recovery lengths for counter-rotating CFT pairs in a wind farm have been found to be around six times the diameter, significantly lower than those typical for AFTs. Using velocimetry data, multiple researchers have highlighted the asymmetry of the wake in the cross-section perpendicular to the blade span [70–73], and the significance of blade tip vortices in wake recovery [71,72,74–76]. Computations with RANS [62] and LES [75,77] modeling have also corroborated these observations. In Ref. [75], higher turbulence intensities have been found to enhance entrainment and recovery by distorting and breaking down the three-dimensional vortex structures in the wake. Ref. [78] examines the distinct streamwise velocity profiles in the wake for different tip speed ratios. LES is the more popular choice of modeling to investigate CFT wakes, often combined with low-order models for computing forces on the fluid from the turbine blades [79–83]. To the author's knowledge, a direct comparison of the wake flow field between RANS and LES has not been investigated. Considering the ubiquitous nature of 2D RANS modeling in simulation of CFTs due to its low computational cost, a direct comparison with LES will help to elucidate the role of RANS models in terms of strengths and limitations in predicting performance and the unsteady flow physics.

The turbine geometry and Reynolds number in this paper match previous experiments performed in a water flume with highly confined flow involving walls on three sides and a free surface [16]. It is well established that CFTs experience enhanced power generation in confined flow [17,18], and to take advantage of this, they may be deployed in areas with

natural flow constrictions such as in shallow or narrow channels. When comparing LES to RANS modeling for a CFT [57,64], the effect of confinement has not been examined in past literature. Thus, the goal of the present paper is to perform high-fidelity wall-resolved LES of a CFT with geometry and flow conditions matching previously reported RANS and experiments, while particularly investigating the interaction of confinement with the modeling technique. The strengths and limitations of LES and 2D RANS in modeling the dynamic stall process and the turbine wake in confined flow are examined, and compared to results in unconfined flows.

3.2 Confined configuration

The confined configuration simulates a blockage ratio of 10.6%, similar to the prior experiments by Snortland et al. [16] with a matching turbine geometry and a blockage ratio of 11.6%. The angle of attack and relative velocity variation for $\lambda = 1.9$, calculated with equation (1.2) and equation (1.3), is presented in figure 3.1a. The phase-averaged power and forces from LES are compared with RANS computations [84] in figure 3.1b for a single blade of the turbine, and also with the experiments [16] in figure 3.1c for a total of both blades. The mean power coefficient from LES is 0.309, from the RANS computation is 0.454, and from the experiment is 0.377.

The C_P for RANS reaches its peak around 5° later than that for LES. While the peak for the experiment lies in between them, around $\theta = 105^\circ$, considering the relatively lower time resolution of the experimental data, it seems to be more in phase with the LES. The power coefficient for LES is significantly lower compared to RANS after $\theta = 90^\circ$ as the upstream power-generating blade starts experiencing angles of attack higher than 20° and decreasing relative flow speeds. This offset between RANS and LES remains almost constant while there is no difference between the two in the power loss on the downstream blade during

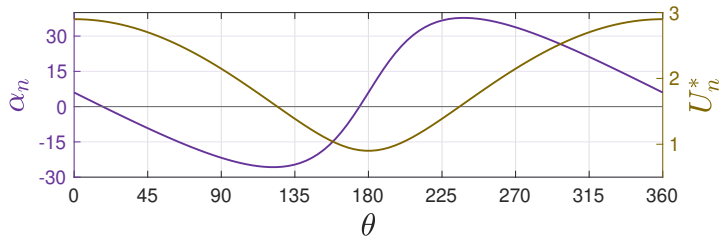

(a) Variation of angle of attack and relative velocity for $\lambda = 1.9$, computed by equations 1.2 and 1.3.

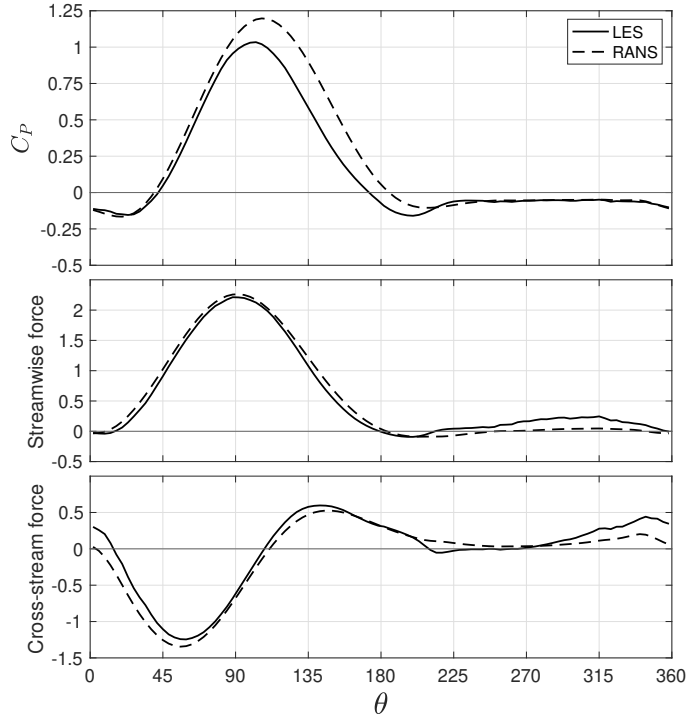

(b) Single blade data from simulation (averaged over both blades).

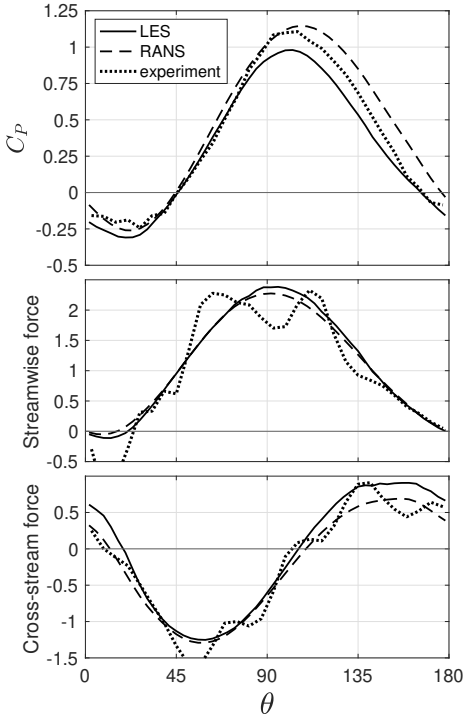

(c) Sum of both blades, compared with experiment.

Figure 3.1: Comparison of power coefficient and force coefficients from experimental data (blockage ratio = 11.6%), and from RANS and LES (blockage ratio = 10.6%) for $\lambda = 1.9,\ Re = 4.5 \times 10^4$.

this period (after $\theta = 270°$). The offset starts reducing and ultimately disappears only after the blade stops generating power.

The LES under-predicts C_P as compared to the experimental data, but the offset between the two curves starts reducing after around $\theta = 135°$. While single blade data from this experiment is not available, data from a similar experimental setup [15] with a single blade turbine suggests that this reduction in the gap may be due to an increasing power loss from the downstream blade after $\theta = 315°$ in the experiment. It is relevant to note that while

the cross-sectional blockage ratio in the experiment is 11.6%, this considers both the width and span of the flume in the y-z plane. The computations impose a blockage of 10.6% only across the width (y-direction). The equivalent blockage in the experiment, that is the ratio of turbine diameter to flume width, is 23%, which is a probable reason for the difference in the peaks between LES and experiment.

In addition to the torque/power generated, the streamwise and cross-stream forces on the blades are also presented as they affect fatigue in turbines. In the experimental data reported, there exist large fluctuations in the forces. Since the simulation has no support structure, the forces on the blade are calculated from the experimental force measurements by subtracting out the forces on the support structure rotating without a blade. The fluctuations are likely due to a mechanical-hydrodynamic resonance of the experimental setup. Nonetheless, the values within the simulation compare well to the mean values of the experiment. However forces on a single blade from the computations demonstrate how periods of small differences in the forces can have large differences in the torque generation, such as from $\theta = 90^\circ$ to 180°, and that periods with no difference in the torque on the blade may have differences in the forces, such as after $\theta = 225^\circ$. Hence subtle differences in the pressure distribution on the blade cannot be extrapolated from observing the magnitude of forces on the blade.

Figure 2.5 shows a comparison of phase-averaged particle image velocimetry (PIV) data from the experiment [16] and the phase-averaged flow field from LES and RANS. At $\theta = 102^\circ$, the angle of attack is approximately 24° (figure 3.1a) which is higher than the stall angle for a stationary NACA0018 blade. However, no flow separation is observed, presumably due to a combination of the dynamically increasing angle of attack which tends to delay the occurrence of stall, and the effect of confinement. As observed in figure 3.1c, the power generation is at its peak for LES and experimental data, but premature for RANS. While the angle of attack increases by a small magnitude to its maximum of 26° at $\theta = 120^\circ$, the relative flow speed is rapidly decreasing. Whereas this causes flow separation

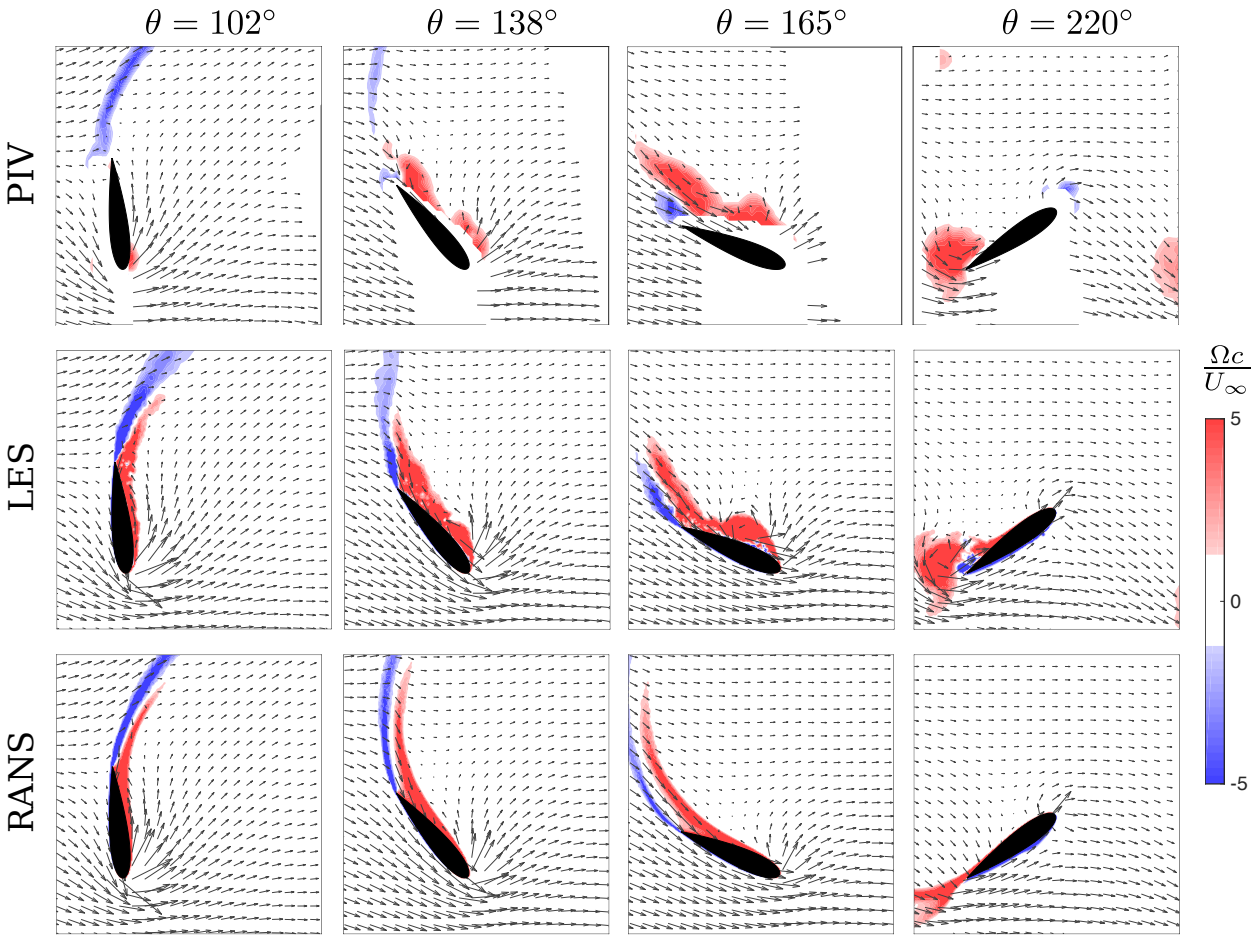

Figure 3.2: Phase-averaged flow velocity (vectors) and vorticity (contours) from experimental data and computations for the confined configuration. $\lambda = 1.9,\ Re = 4.5 \times 10^4$.

observed in the PIV and LES flow field at $\theta = 138°$, the RANS computations suppress flow separation, explaining the delayed peak of C_P and consequently the constant positive offset relative to LES. The separation region near the trailing edge in PIV and LES skews the force vector on the blade towards it, reducing power generation. However, the flow fields do not adequately explain the gap between the C_P from experiment and LES which gets smaller as the blade is completing its motion on the upstream side.

As the upstream blade moves further, a leading edge vortex (LEV) is created and shed as seen at $\theta = 165°$ and $\theta = 220°$ in the PIV and LES fields, but no LEV is observed in the RANS field indicating complete suppression of flow separation. Figure 3.3 demonstrates the instantaneous vorticity field for LES and RANS at four different positions of

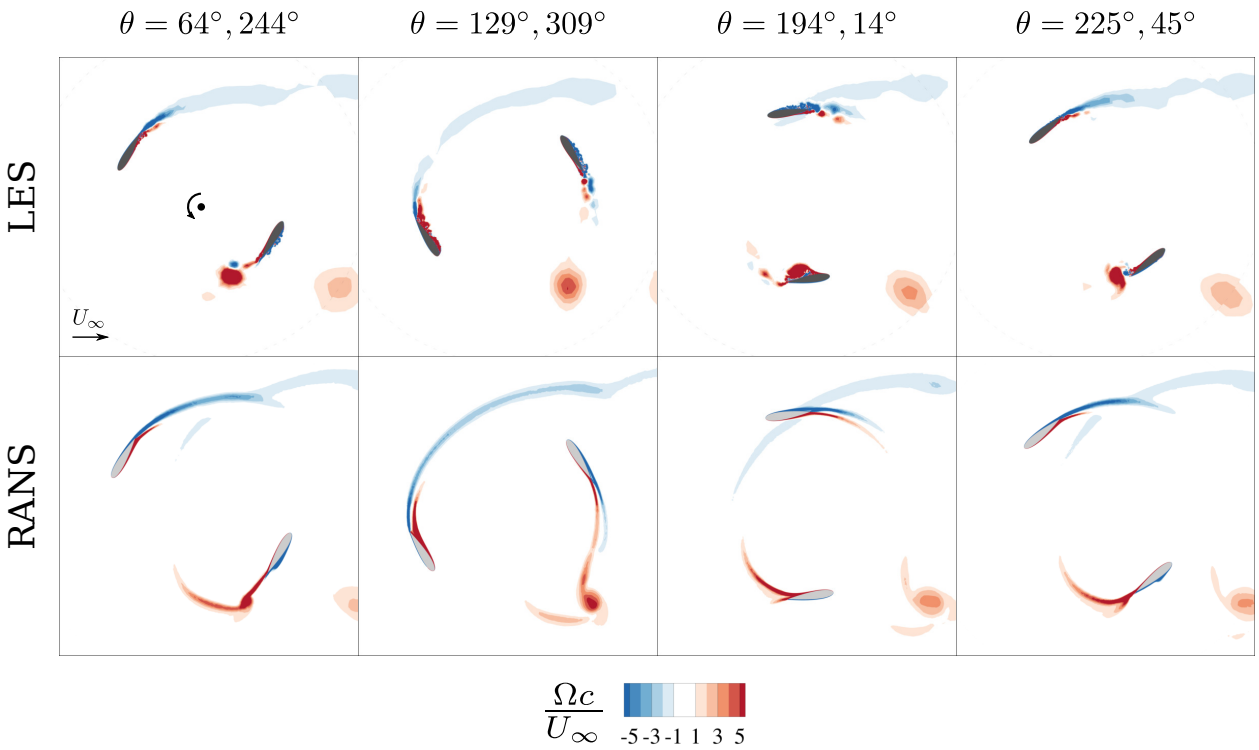

Figure 3.3: Instantaneous vorticity fields from LES (span-averaged) and RANS for the confined configuration. $\lambda = 1.9,\ Re = 4.5 \times 10^4$.

the turbine with both blades in the frame. A distinct separation region having small scale flow structures is observed at the blade for LES compared to a smooth boundary layer for RANS, demonstrating its limitations in modeling separating flow as noted in past research [57–59, 64, 65]. While a relatively weak trailing edge vortex (TEV) is created in RANS far after the blade has completed its upstream motion, the LES field shows a stronger LEV created on the blade due to flow separation.

3.3 Unconfined configuration

The unconfined configuration allows free outflow from all boundaries except the inlet, simulating conditions with no walls or free surfaces at a distance close enough to affect the flow around the CFT blades. Such conditions may be found while harvesting wind energy or in sufficiently wide and deep water channels and is analyzed here as a reference

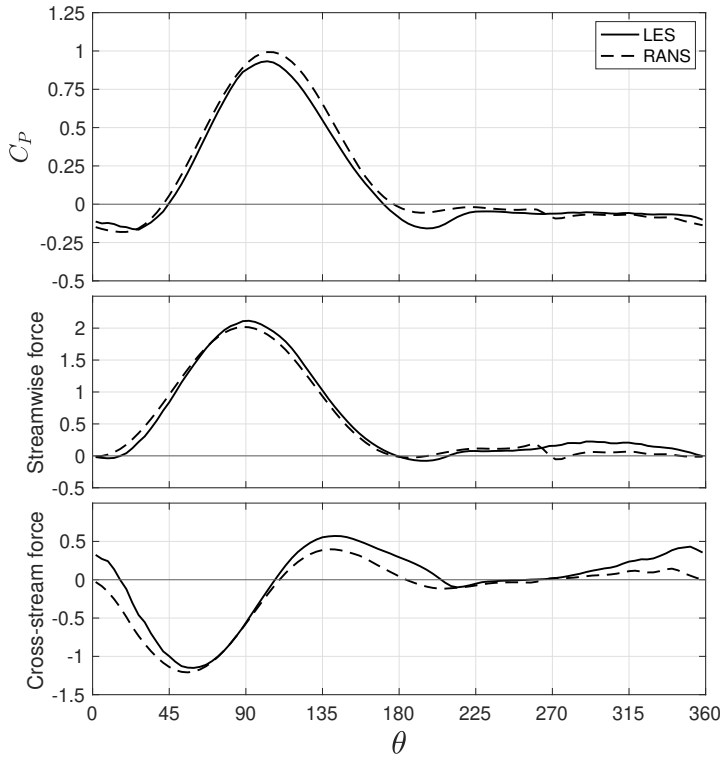

Figure 3.4: Power coefficient and force coefficients from RANS simulation (blockage ratio = 1.7%) and LES (unconfined) for $\lambda = 1.9,\ Re = 4.5 \times 10^4$.

for comparing the results from the confined configuration. figure 3.4 shows a comparison between the LES and RANS computations for power and forces on a single blade with an unconfined configuration. The mean power coefficient from LES is 0.264 and from the RANS computation is 0.324. The power coefficient for the experiment, when corrected for the blockage using Barnsley and Wellicome's method [18, 43], reduces to 0.305. The power generation from LES is reduced by 14.6% as compared to the confined configuration whereas that for RANS is reduced by 28.6%. Comparing with figure 3.1b, the power coefficient curve from LES undergoes a subtle drop in the peak while the RANS curve sees a more significant reduction. The RANS curve also undergoes a shift in its peak and is more in phase with LES for the unconfined configuration rather than being delayed. As the blade advances there is a small offset between the two curves throughout its upstream motion. However a more notable difference can be observed between $\theta = 180°$ and $220°$.

Figure 3.5 compares the vorticity for the unconfined RANS and LES computations.

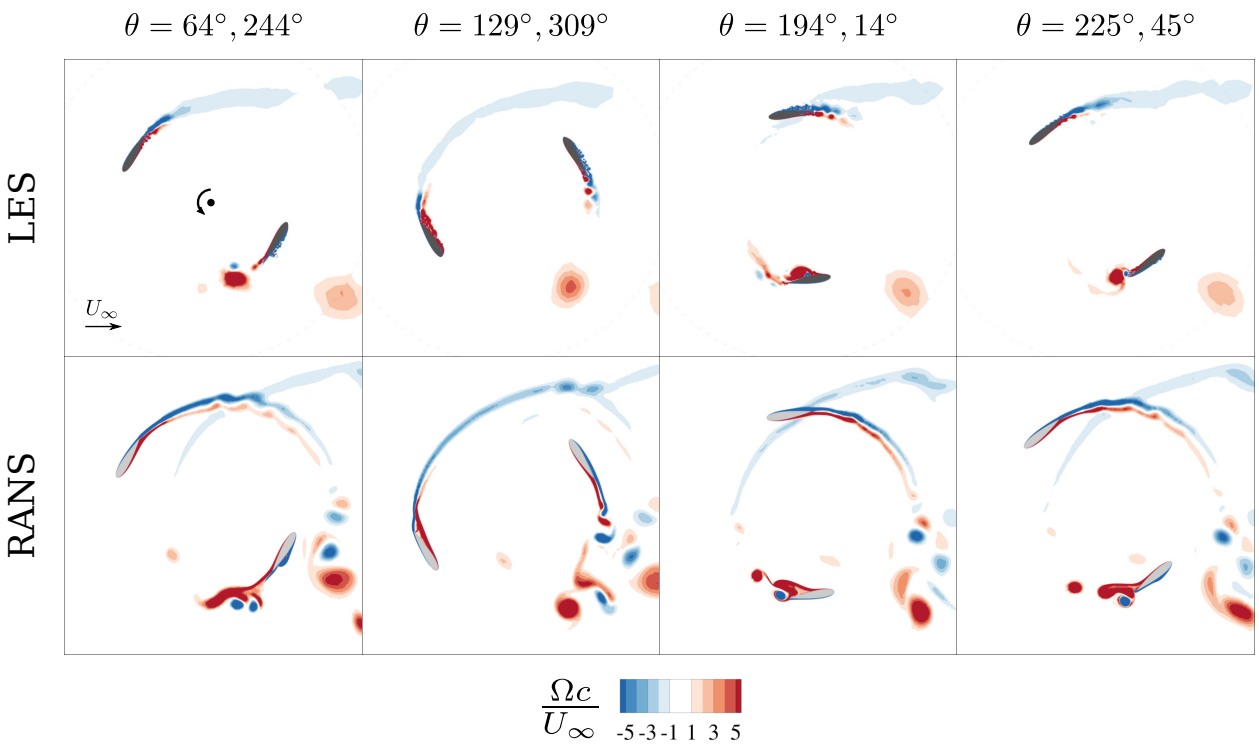

Figure 3.5: Instantaneous vorticity fields from RANS and LES (also span-averaged). Blockage ratio = 10.6%, $\lambda = 1.9,\ Re = 4.5 \times 10^4$.

Unlike the confined flow, the RANS does have flow separation at $\theta = 129°$ but no distinct LEV formation and roll-up like the LES. This observation is a probable reason for the small offset between the two curves from $\theta = 100°$ to $\theta = 180°$, as the force vector on the blade is turned towards the trailing edge due to the more pronounced separation in LES. A significant difference can be seen as the LEV is forming and leaving the blade at the end of its upstream motion from the vorticity fields at $\theta = 195°$ and $\theta = 225°$. The RANS computation shows a dynamic stall vortex leaving the blade surface while a shear layer is still rolling up, along with the formation of a trailing edge vortex. The LES however shows a single coherent vortex forming at the blade and leaving it at a later azimuthal position compared to RANS, and as a consequence reducing the power generation from $\theta = 180°$ to $220°$ as observed in figure 3.4.

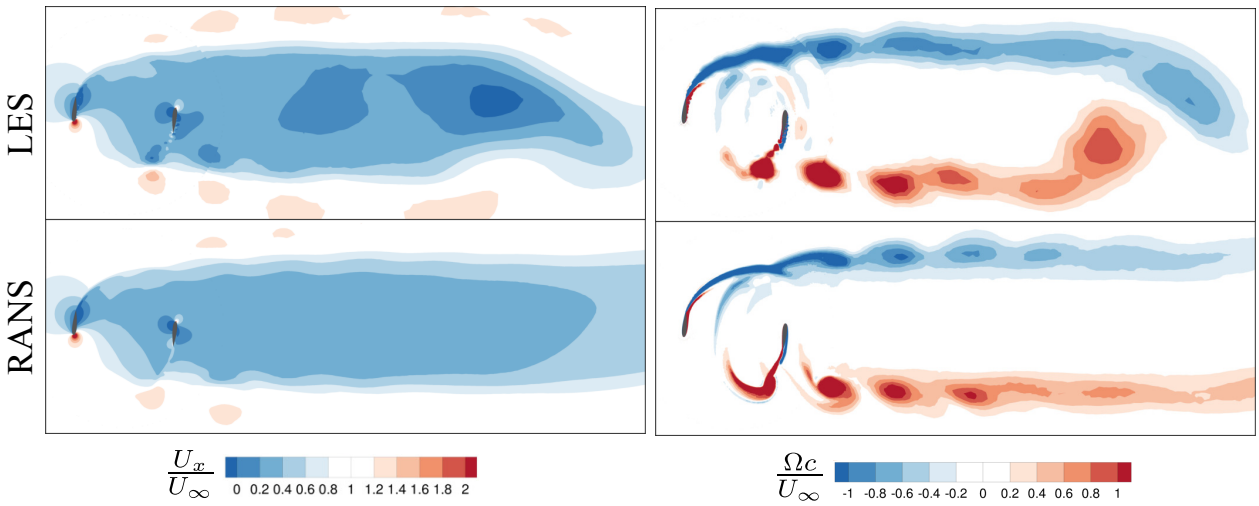

Figure 3.6: Instantaneous streamwise velocity and spanwise vorticity from LES (span-averaged) and RANS for the confined configuration. $\lambda = 1.9,\ Re = 4.5 \times 10^4$.

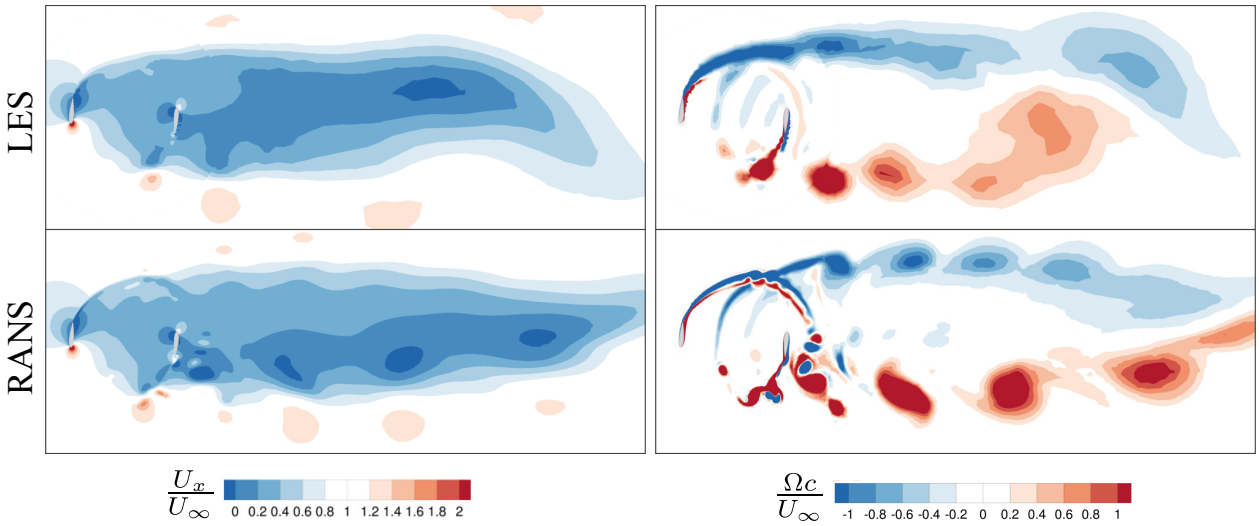

Figure 3.7: Instantaneous and span-averaged streamwise velocity and spanwise vorticity fields from RANS and LES (unconfined) for $\lambda = 1.9,\ Re = 4.5 \times 10^4$.

3.4 Wake dynamics

The differences in near-blade vortex dynamics will also affect the wake of the turbine and hence the performance and tuning of downstream turbines in array configurations. Figure 3.6 presents the streamwise (along x) velocity and the spanwise (along z) vorticity in the wake for the confined configuration. The stronger counter-clockwise LEVs produced in LES around $\theta = 180°$ (leeward side of the turbine) as explained in section 3.2, convect

along the edge of the wake. Additionally, a stronger clockwise vorticity is also shed by the blades in the LES around $\theta = 0^\circ$ (windward side) that travels along the wake. The direction of vorticity on both the windward and leeward sides and their mutual induction tends to reduce the x-velocity in the core of the wake. This *self-induction* of the wake and the resulting higher velocity deficit in the core causes the counter-clockwise LEV at the leeward side to get entrained into the core resulting in an asymmetric wake. The RANS model on the other hand, shows a more symmetric wake structure due to the absence of strong LEVs from the blades, with a lower local velocity deficit distributed over a larger width. Multiple research works have highlighted asymmetry of the wake through velocimetry data [70–72] and computations [62,75,78] while proposing varying explanations [73]. The self-induction of the wake has also been cited as a reason for increase in the asymmetry as the wake advances downstream [72].

The wake flow fields for LES with the unconfined configuration in figure 3.7 show a similar profile as the confined configuration in figure 3.6, apart from a larger numerical dissipation due to a coarser mesh. For RANS, stronger vortices are created at the leeward side leading to an unsteady wake in contrast to the symmetric, steady wake in figure 3.6. A notable contrast observed between the LES and RANS fields is that while the vortices traveling at the leeward side of the turbine in LES get entrained into the wake due to self-induction, the vortices in RANS continue traveling further downstream with a smaller deviation from their prior path. Comparing the vorticity and velocity images, it appears that these vortices do not significantly affect the velocities in the core of the wake, away from their immediate area of influence.

While additional numerical dissipation occurs in the wake due to a coarser mesh resolution compared to the interior of the turbine, a wall-resolved computation at the blades allows tracking the differing evolution of vortices and consequently the wake structure. The distinct separation region, the premature shedding of the LEV, and the lack of mutual induction or diffusion of vorticity in the wake may be attributed to the two-dimensional

nature of the RANS modeling that does not account for the three-dimensional dynamics of turbulence and vorticity. However, previous research has also highlighted the inaccuracies of three-dimensional RANS models in realistically describing the separation and vortex structures on CFT blades, as compared to higher-fidelity models [64–67].

3.5 Turbine pair under high confinement

Natural confinement in river or tidal flow can be exploited to increase power generation by employing multiple CFTs. A project is underway to investigate the feasibility of reducing the levelized cost of energy for deploying this technology in the field, which involves a multi-disciplinary co-design cycle involving experiments, simulations, structural analysis, electrical design, environmental and market analysis. Unsteady RANS computations are employed to estimate performance and forces for a turbine pair with a low turn-around time.

Two CFTs with a center to center distance of $1.2D$, where $D = 2R$, are simulated rotating in opposite directions such that the blades travel downstream along the center line between the turbines. The turbines have identical tip speed ratios and blade azimuthal positions with respect to the oncoming flow. This configuration helps cancel the cross-stream forces acting on the mounting structure hence reducing the material usage and cost.

The turbine in experiments presents a blockage on a two-dimensional cross-section along both the width and span of the turbine. The computations however present a one-dimensional blockage only across the width. Kinsey & Dumas [17] explore the effect of asymmetry in blockage along the two directions using 3D simulations along with comparing the limiting case of 2D simulations. An asymmetry ratio of 4 between the blockages along width and span is found to have an effect of up to 7% on power at a total blockage of 26%. This project however simulates higher confinement.

The initial design cycle includes turbine pair experiments in the above configuration

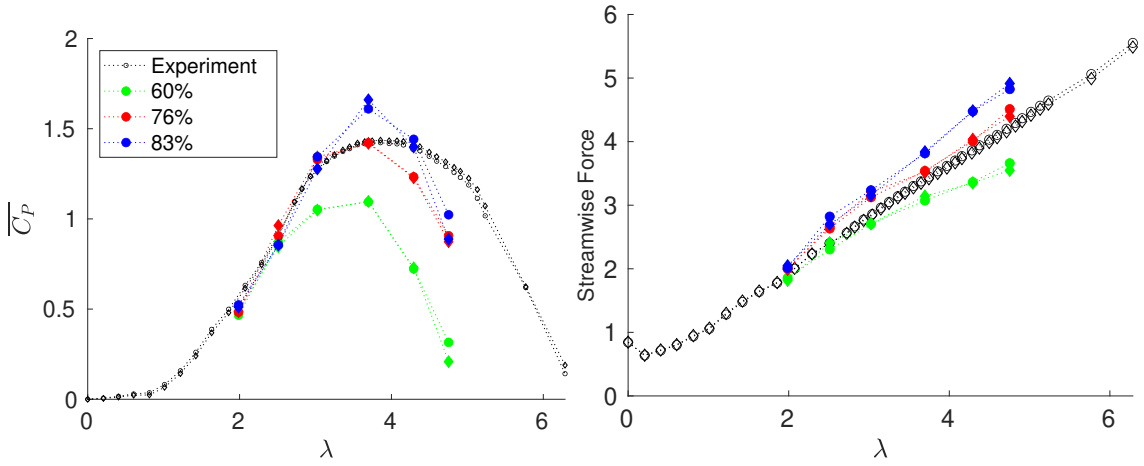

Figure 3.8: Time-averaged power and streamwise force coefficients from unsteady RANS simulations of the turbine pair system. Each of the two marker shapes represent the total force on each of the two turbines.

with a width-based confinement of 83% and span-based confinement of 72% resulting in a cumulative blockage of 60%. Hence a sweep of unsteady RANS simulations over a range of tip speed ratios is run with blockage ratios of 60% and 83% to test whether the experimental outcome can be reproduced better using merely the width-based or the cumulative blockage. Figure 3.8 compares the time-averaged power and streamwise force coefficients. In the optimal range of rotation rates, the power and force are over-predicted with 83% blockage and under-predicted with 60%. Based on a linear interpolation of the power at $\lambda = 3.7$, a third confinement of 76% is simulated which successfully predicts the time-averaged performance on the lower end of the rotation rates. However beyond $\lambda = 4.2$, all three confinements under-predict the power while the streamwise force is represented accurately, demonstrating the volatility of RANS modeling.

Figure 3.9 shows the phase- and blade-averaged power generation for one of the turbines, representing the per-blade performance at two rotation rates in the sub-optimal and optimal range. Whereas the time-averaged power matches for all three confinements at $\lambda = 2.5$, the peak power in the cycles in lower for 60% blockage which is compensated for in the downstream part of the cycle. The $\lambda = 3.7$ power cycles clearly show the increasing power generation with confinement.

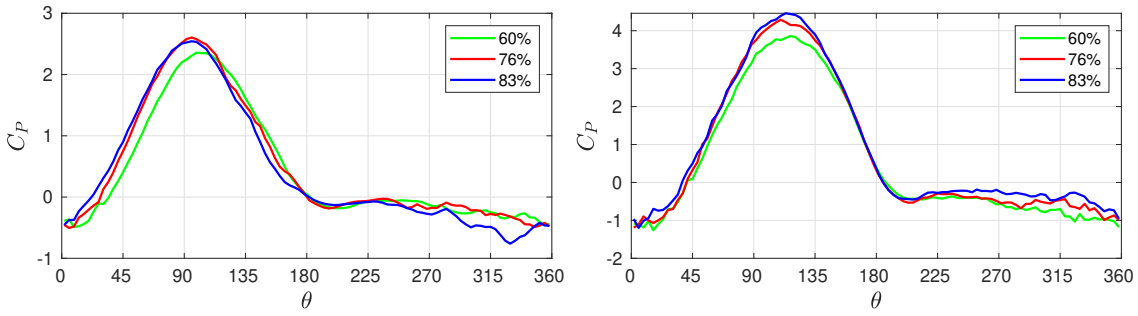

Figure 3.9: Phase-averaged per-blade power generation for $\lambda = 2.5$ (left) and $\lambda = 3.7$ (right).

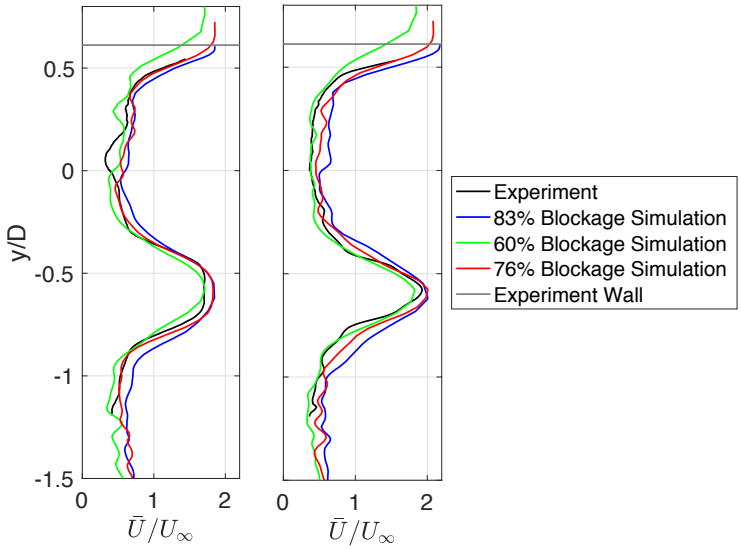

Figure 3.10: Time-averaged streamwise velocity at the streamwise position of $\Delta x/D = 0.59$ from the turbine centers for $\lambda = 2.5$ (left) and $\lambda = 3.7$ (right). $y/D = 0$ represents the cross-stream position of the top turbine.

An effective method of comparing the response of the turbines under varying confinement between simulation and experiment is to analyze the near-wake velocity, especially the bypass velocities between the two turbines and between the turbine and wall. The time-averaged values are displayed in figure 3.10, where the increasing turbine-wall bypass velocity demonstrates the trend of increasing confinement. The 76% blockage simulation matches this bypass velocity to the experiment.

While the performance metrics are of interest to the co-design cycle, the flow field prediction is presented in figure 3.11 to observe the capability of the RANS model. The rotation rate of $\lambda = 2.5$ is used since the blades are expected to experience flow separation due to

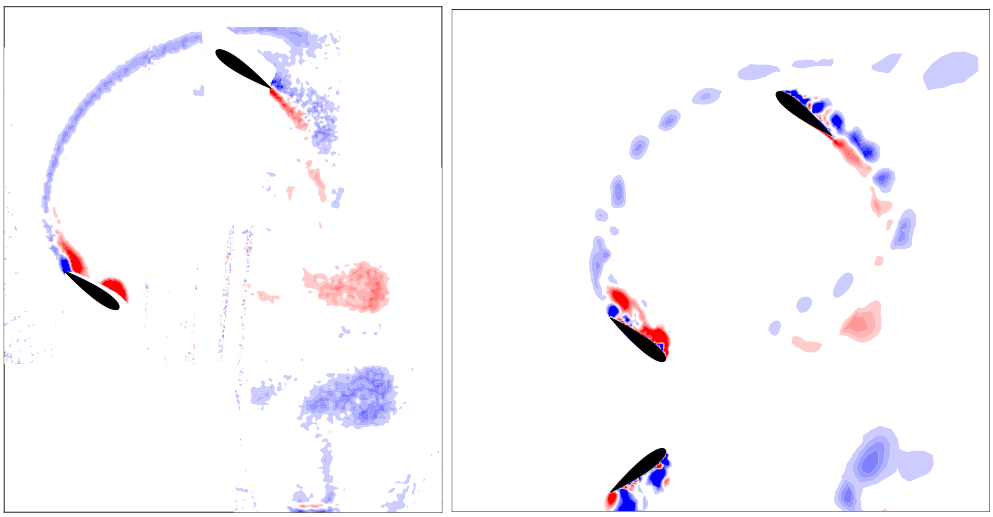

(a) $\theta = 150°$

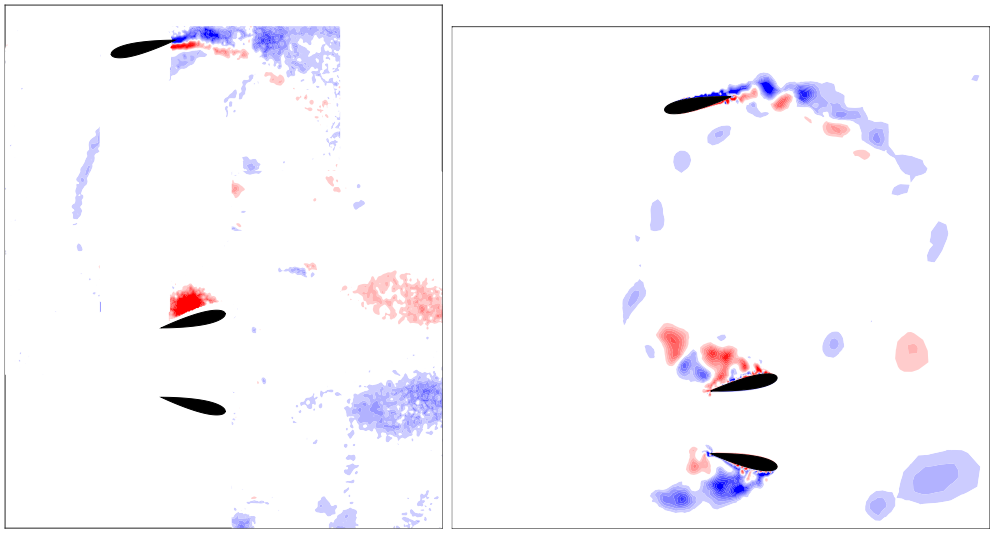

(b) $\theta = 198°$

Figure 3.11: Phase-averaged vorticity fields at two azimuthal positions from experiment (left) and the RANS simulation with 76% blockage (right) for $\lambda = 2.5$.

higher angles of attack. The LEV formation on the blade is represented accurately in the simulation. However after detachment, the phase-averaged vorticity from the simulation does not show a fully coherent vortex due to cycle-to-cycle variations in its position and only three averaging cycles as compared to tens of cycles for the experiment.

To further assess the instantaneous flow prediction by RANS, it is compared to LES computations and the experiment in figure 3.12 for 60% blockage at $\lambda = 3.7$. The LES shows a delay in the peak power by about $5°$ as compared to both the RANS and experiment.

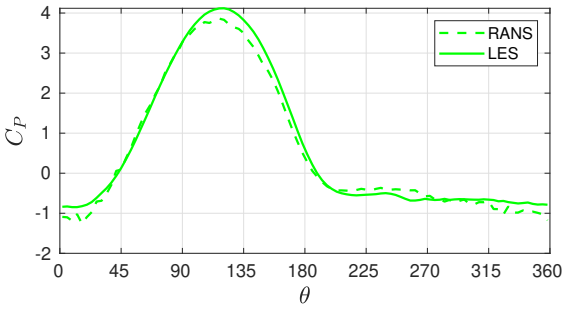

(a) Phase-averaged per-blade power coefficient.

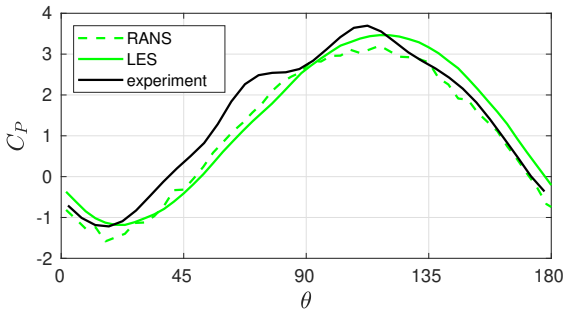

(b) Phase-averaged power coefficients from both blades of a turbine.

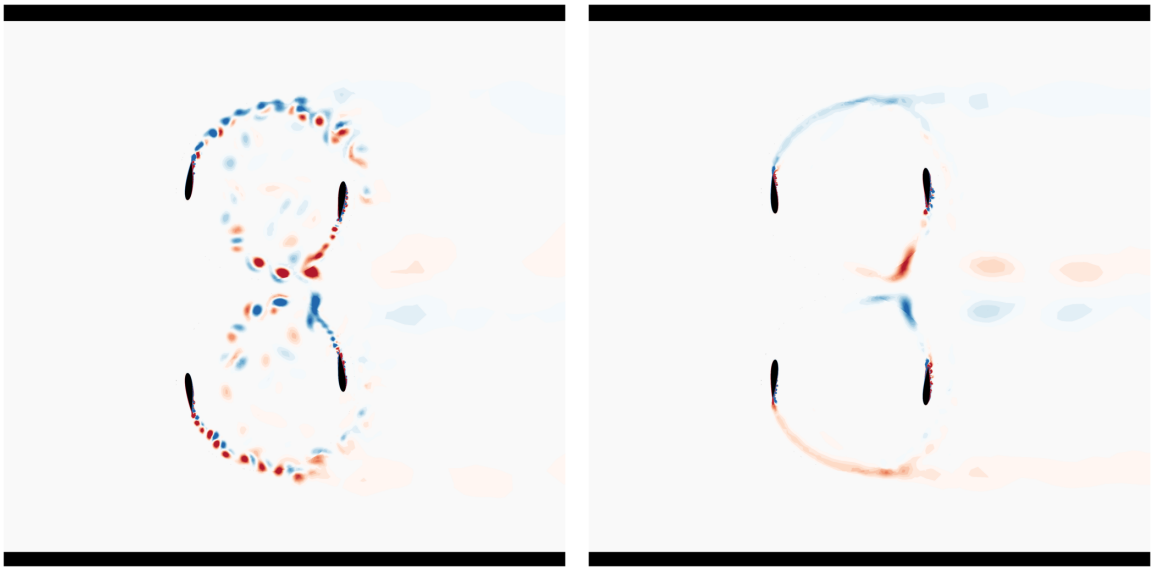

(c) Instantaneous vorticity fields from RANS (left) and LES (right).

Figure 3.12: Comparison of loads and flow fields from RANS and LES at 60% blockage and $\lambda = 3.7$.

However, both LES and RANS yield a lower power until the peak as compared to the experiment. The mean power coefficient is 1.1 from RANS, 1.3 from LES, and 1.43 for the experiment. In contrast, both RANS with a mean C_P of 1.66 and LES with 2.23 overestimate the power as seen in figure 3.13. The instantaneous vorticity fields in figures 3.12 and 3.13 shows spurious vortex shedding from the RANS computation as compared to a single vortex shed for the LES at the end of the power generating phase. Since the RANS model was tuned for a lower confinement and a lower range of tip speed ratios, higher local Reynolds numbers may partly explain this outcome.

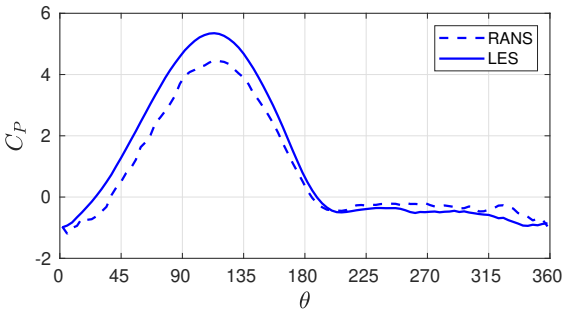

(a) Phase-averaged per-blade power coefficient.

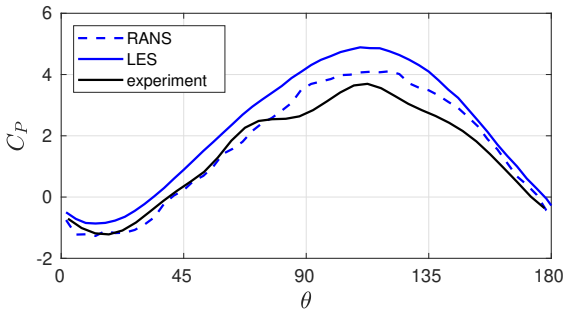

(b) Phase-averaged power coefficients from both blades of a turbine.

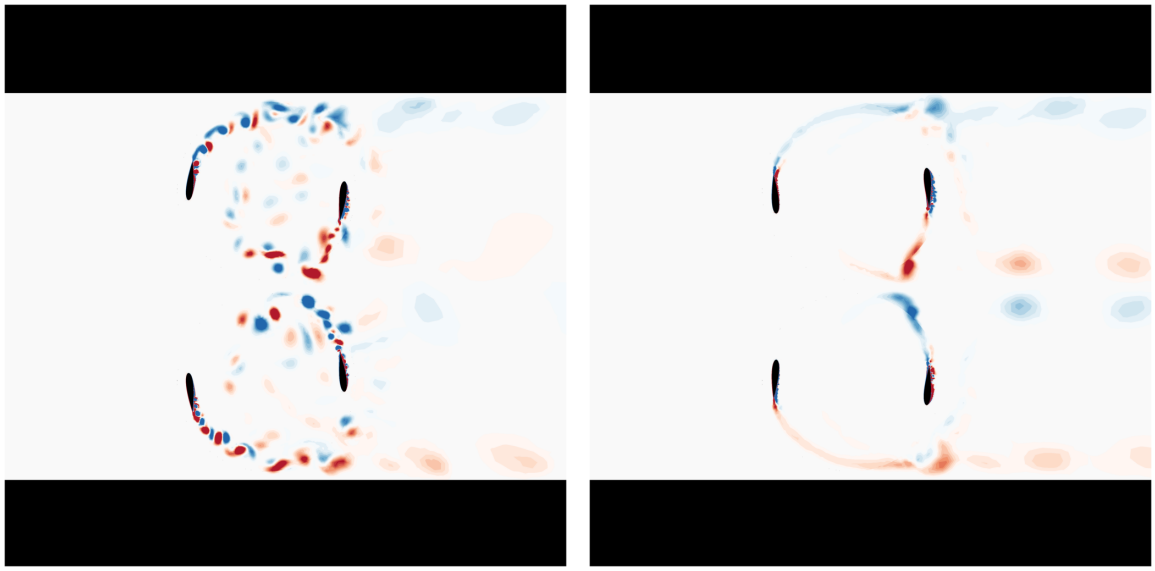

(c) Instantaneous vorticity fields from RANS (left) and LES (right).

Figure 3.13: Comparison of loads and flow fields from RANS and LES at 83% blockage and $\lambda = 3.7$.

3.6 Conclusions

Large-eddy simulations are performed for a straight-bladed cross-flow turbine operating in confined and unconfined flow at a moderate Reynolds number. The flow fields are compared with two-dimensional RANS simulations and velocimetry data from experiment to examine the complex dynamic stall process and evolution of the resulting flow structures, while investigating the interaction of confinement with the modeling technique.

RANS computations exhibit flow separation for the unconfined configuration but completely suppress it for the confined configuration leading to a significant over-prediction

of power generation. LES shows a more subtle rise in power generation for the confined configuration while exhibiting flow separation for both, albeit to a slightly larger extent for the unconfined configuration.

The moderate Reynolds number range, where the modeling of transition from laminar to turbulent flow plays an important role, is not ideal for the RANS model as they are designed for a fully turbulent flow which is insensitive to Re. As presented in chapter 2, in the RANS computations for the unconfined configuration, a significant increase in power is observed with an increase in Re due to the potential suppression of flow separation. While the effects of higher confinement and a higher Re are not perfectly equivalent, they demonstrate the high sensitivity of the RANS model to flow conditions.

A notable difference is observed in the evolution of the separation region at the blade during dynamic stall and a premature shedding of the leading edge vortex is observed in RANS relative to LES. Furthermore the vortices in LES cause self-induction of the wake, increasing the velocity deficit in the core, and consequently getting entrained into the wake. Such self-induction is not observed in the RANS computations for unconfined configuration where vortices in the wake do not appear to impact flow outside their immediate area of influence, showing the differences in vorticity diffusion from LES. Despite these differences, the RANS model provides a good estimate of turbine performance for the unconfined configuration.

The RANS model is also employed to simulate a turbine pair under high confinement over a range of rotation rates. To resolve the discrepancy between the 2D and 3D blockages in simulation and experiments respectively, an adjusted blockage ratio of 76% is determined that matches the experiments with a cumulative 3D blockage of 60% and a width-based blockage of 83%. While the performance and flow physics are well predicted for lower rotation rates up to the optimal range, the power generation is significantly under-predicted at higher tip speed ratios, reinforcing the sensitivity to the local Reynolds number through a comparison of the instantaneous flow with LES of a similar configuration.

4 Modal analysis of dynamic stall development

4.1 Literature review: dynamic stall and modal analysis

Past research has characterized the phases of dynamic stall on the basis of force and moment acting on an airfoil in correlation with temporal evolution of the velocity field and corresponding flow structures. Carr [85] reviews research on dynamic stall and the effect of different kinematic or flow parameters while providing a general chronology for the separation process and the aerodynamic load evolution. The onset of stall is traditionally determined by deviations in the force, suction pressure, or moment coefficients as reviewed by Sheng et al. [86]. In contrast to the explicit use of aerodynamic loads, Mulleners & Raffel [28] define the instance when the primary stall vortex detaches from the leading edge as an onset of its stalled phase. Proper orthogonal decomposition (POD) of the velocity field data from experiment is used to identify the stall onset angle as the instance when the mode coefficient representing the dynamic stall vortex reaches a local maximum. Light and deep stall are defined based on whether the foil starts pitching down before or after the stall onset. Modal analysis of surface pressure distribution from a pitching foil has also been employed to compare the flow trajectories across a parameter space [87] or to examine a bimodal distribution in cycle-to-cycle variations [88].

A foil that is only pitching is inadequate to understand stall on the CFT blade which experiences unsteady relative velocity magnitudes in addition to the varying angle of attack. A pitching foil that is simultaneously plunging, surging, or experiencing unsteady freestream flow is explored in literature for applications to helicopter blades [89], gusts [90], energy harvesting or propulsion [91–94], and cross-flow turbines [95]. The plunging motion for a range of kinematics delays the detachment or convection of the LEV and

enhances lift [89,92]. Gharali & Johnson [96] explore the effects of amplitude and phase difference of an unsteady freestream flow on a pitching foil. Relevant to the cross-flow turbine, it is shown that a freestream varying out-of-phase to the pitching motion can result in loads lower than from a static stall. It is also established by Wong et al. [90] that a moving foil experiences a different force history from an unsteady inlet flow with identical relative velocity variation due to fluid acceleration and the distribution of vorticity at the trailing edge. Dunne & McKeon [95] extrapolate a low-order model using the first five dynamic mode decomposition (DMD) modes from a pitching-surging foil to estimate the flow around a rotating CFT blade.

A CFT blade rotating on an axis perpendicular to the flow experiences distinct conditions in the form of flow curvature along blade chord and undefined oncoming flow direction due to induced flow. Research on a pitching, plunging, or surging foil generally investigates one side of the blade due to a non-zero mean angle of attack or a symmetry between two halves of the stall cycle. In contrast, for a CFT blade, the suction side switches during the downstream half of its rotation, and encounters low velocity flow due to energy extraction that alters the stall cycle and presumably influences the upstream half due to history effects. In addition, Coriolis forces on the flow play a crucial role, particularly in determining the position of the stall vortex which is not adequately modeled by a pitching-surging blade with identical relative flow [14].

For estimating the aerodynamic loads and turbine performance using low-fidelity models, the effects of flow curvature have been studied [97–101]. A symmetric CFT blade with high chord-to-radius ratio behaves like a cambered foil in aligned flow with an incidence angle shift that effectively modifies the angle of attack computed geometrically at a single point. Horst et al. [102] compare different airfoil transformation methods from literature which theoretically calculate this virtual camber and incidence angle, finding that all methods produce similar results up to a chord-to-radius ratio of 0.4.

Analyzing aerodynamic loads at the blade level allow a comparison with dynamic stall

research on non-rotating foils. Bianchini et al. [103] show that the CFT blade pitching moment causes an asymmetry in the starting torque between the upstream and downstream side, and explore the ideal location for blade-spoke connection based on the moment variation. Le Fouest et al. [29] develop a methodology to automatically characterize the stall cycle across multiple rotation rates based on POD modes of vorticity and aerodynamic loads from experiments of a one-blade CFT. The on-blade flow physics have also been investigated with a frequent emphasis on the formation and evolution of the stall vortex [25, 26]. However, a direct association of force or pitching moment with the stall vortex dynamics in perspective of the above-mentioned factors that distinguish a CFT blade from non-rotating ones is missing in literature.

Modal analysis techniques such as POD or DMD that project the unsteady flow field onto a linear subspace are commonly used for analysis [104, 105] or control strategies [106–108] for dynamic stall due to their simplicity of implementation. With application to CFT, while modal analysis has been used to examine the wake topology [73, 109], it has not been implemented at the blade level except in [29]. This is presumably due to the difficulty of acquiring a full circumferential field of view around the blade throughout the rotation in experiments and the challenge posed by a moving reference frame to the pre-processing of flow data. This research uses POD to investigate the temporal evolution of the most energetic modes while associating it with the stall process and to compare distinct kinematics through a common set of modes.

Much of the literature on CFT focuses on performance optimization over geometry or control parameters [15, 110, 111] and system level analysis of the flow such as the wake topology [61, 62, 73, 76, 78, 80, 81] or turbine array performance [20, 69, 112–114]. The aim of this work is to analyze stall development and onset at the blade with potential application to flow control strategies and highlight analogous or contrasting phenomenon with past research on a non-rotating pitching or plunging foil. Two distinct stall regimes are investigated: a constant angular velocity rotation that represents the optimal tip speed

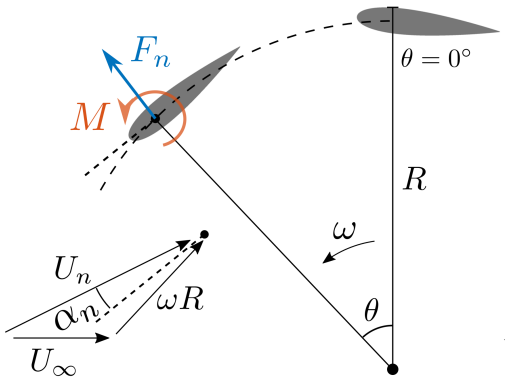

Figure 4.1: Kinematics and aerodynamic loads for the CFT blade.

ratio and experiences moderate angles of attack, and a low angular velocity rotation that causes nominal angles of attack up to $60°$. The dominant spatial modes and their time development coefficients are analyzed in reference to the force or pitching moment on the foil and the evolution of surface pressure and vortices at the blade.

4.2 Methods

Blade aerodynamic loads

The blade loads that are analyzed for characterizing stall are the normal force, F_n, and the pitching moment about the quarter-chord location from leading edge, M, as shown in Figure 4.1. The loads are normalized using the blade velocity, ωR, as the pitching moment coefficient and the normal force coefficient given by

$$C_m(\theta) = \frac{M(\theta)}{\frac{1}{2}\rho\,(\omega(\theta)R)^2\,Sc} \quad \text{and} \quad C_n(\theta) = \frac{F_n(\theta)}{\frac{1}{2}\rho\,(\omega(\theta)R)^2\,S}\,, \tag{4.1}$$

where S is planform area of the blade. The moment, M, is positive in the counter-clockwise (CCW) direction and F_n is positive when acting outward from the turbine as demonstrated in Figure 4.1.

Proper orthogonal decomposition

Ten rotations of the turbine are simulated for $\lambda = 1.9$ and nine for $\lambda = 1.1$ using the wall-resolved LES model described in chapter 2. The first four are eliminated and the last six/five are considered for modal analysis as the flow physics stop changing significantly from one rotation to the next. Flow data at 70 azimuthal positions per rotation for $\lambda = 1.9$ and 121 for $\lambda = 1.1$ provide a total of 840 and 1210 snapshots respectively from the two blades with uniform time intervals.

A low-dimensional basis is constructed for the full circumferential flow field around the rotating CFT blade through proper orthogonal decomposition (POD) implemented on flow data from LES. Span-averaged velocity, normalized by the freestream velocity, is extracted on a grid of resolution $0.01c$ from a region of size $1.5c \times 1c$ centered at the blade for $\lambda = 1.9$. For $\lambda = 1.1$, the field of view is expanded to $2c \times 1.5c$ to include more area on the inside of the blade containing the large stall vortex. To provide a uniform reference frame across time, a velocity field relative to the blade, $\boldsymbol{u}$, is calculated by subtracting the instantaneous blade velocity and the blade position is fixed horizontally (Figure 4.2). Next, the time-averaged mean velocity field is subtracted from all snapshots to obtain the fluctuating component, $\boldsymbol{u'} = \boldsymbol{u} - \bar{\boldsymbol{u}}$. Velocities along x-direction (along the blade) and y-direction (lateral to the blade) on the two-dimensional grid from each time snapshot are then stacked as a one-dimensional column vector, with time advancement along rows of the matrix, known as the method of snapshots [115]. Finally, a singular value decomposition of this matrix provides the spatial modes, $\psi_m(x, y)$, and their time development coefficients, $a_m(t_j)$, such that the flow can be reconstructed as $\boldsymbol{u'}(x, y, t_j) = \sum_{m=1}^{N} a_m(t_j)\psi_m(x, y)$, where m is the mode index in decreasing order of their singular values or significance, and j is the time snapshot index. The mode coefficients are however presented in terms of the azimuthal position, θ_j.

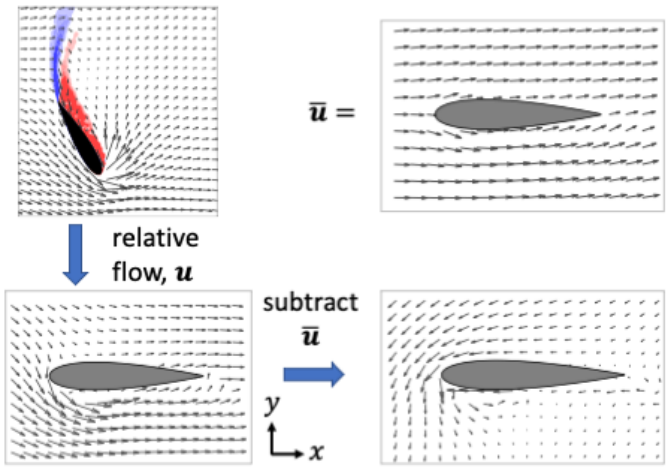

Figure 4.2: Pre-processing of velocity data for POD.

4.3 Results

Modal analysis of optimal TSR, $\lambda = 1.9$

For the geometric configuration and Reynolds number regime in this research, $\lambda = 1.9$ represents the optimal constant rotation rate. Whereas the torque generation and flow field were previously analyzed qualitatively in chapter 3, this research focuses on a blade level analysis of the stall cycle by associating the flow physics with surface pressure, normal force, pitching moment, and POD modes.

Figure 4.3 presents the first four modes from POD as x-velocity fields where the x-direction is along the blade chord, and the bottom of the foil corresponds to inside of the rotating blade that is facing the turbine center. The respective time development coefficients are displayed in the bottom frame of Figure 4.4. The nominal relative flow metrics α_n and U_n^*, the instantaneous aerodynamic loads C_n and C_m, and the torque C_Q are also plotted from the last rotation of one of the two blades.

Mode 1 represents flow along the blade chord with some differences between the outside and inside of the blade as well as closer to the blade due to the lift generation. Hence its temporal coefficient closely imitates the relative velocity magnitude U_n^* on the upstream side from $\theta = 0°$ to $180°$ as seen in Figure 4.4 . It also shows an asymmetry

between the upstream and downstream side most clearly observed after $\theta = 240°$ with the lower magnitudes representing the low velocity of oncoming flow. Mode 2 shows the flow sharply bending around the leading edge hence indicating lift generation and its coefficient matches the torque generation by the blade shown in the top frame in Figure 4.4 in terms of the peak occurring around $\theta = 95°$ and the negative peak around $\theta = 215°$. Modes 3 and 4 prominently include regions of reverse flow at the blade surface along with rotational flow as observed by neighboring regions of opposite signed velocities. Analyzing their time coefficients, the positive and negative peaks show the leading edge vortex formation and shedding.

In Figure 4.4, the pitching moment is negative in the clockwise direction, implying a “pitch-down" moment relative to the angle of attack during the upstream rotation of the turbine, and a “pitch-up" moment relative to the nominal angle of attack during the downstream rotation. Critical points in the cycle are marked by letters a-g and the corresponding instantaneous surface pressure and vorticity fields are presented on the right in Figure 4.4. The pressure is normalized in reference to the pressure at an upstream distance of $12R$ from the turbine center. It is shown as a series of vectors acting along the blade surface normals where a vector acting outward from the blade implies a pressure suction on the surface. The spanwise variation in the pressure field is also observed from the distribution of different lengths at a specific location.

At the start of the upstream motion in Figure 4.4(a), the nominal angle of attack is still

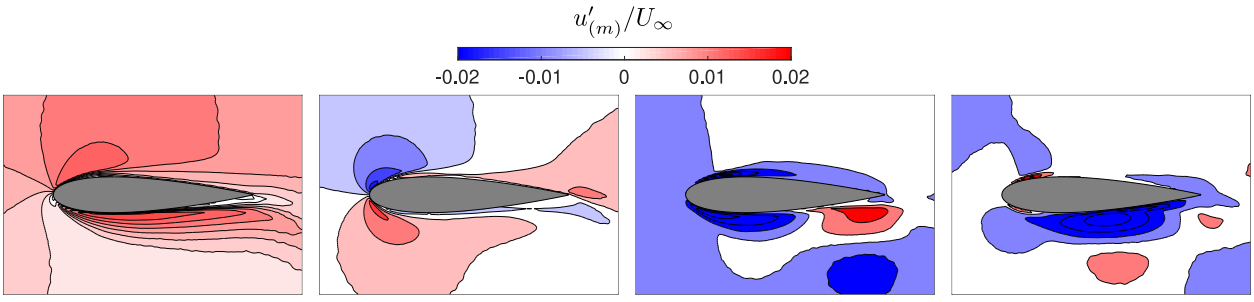

Figure 4.3: Modes as x-velocity fields, for $\lambda = 1.9$.

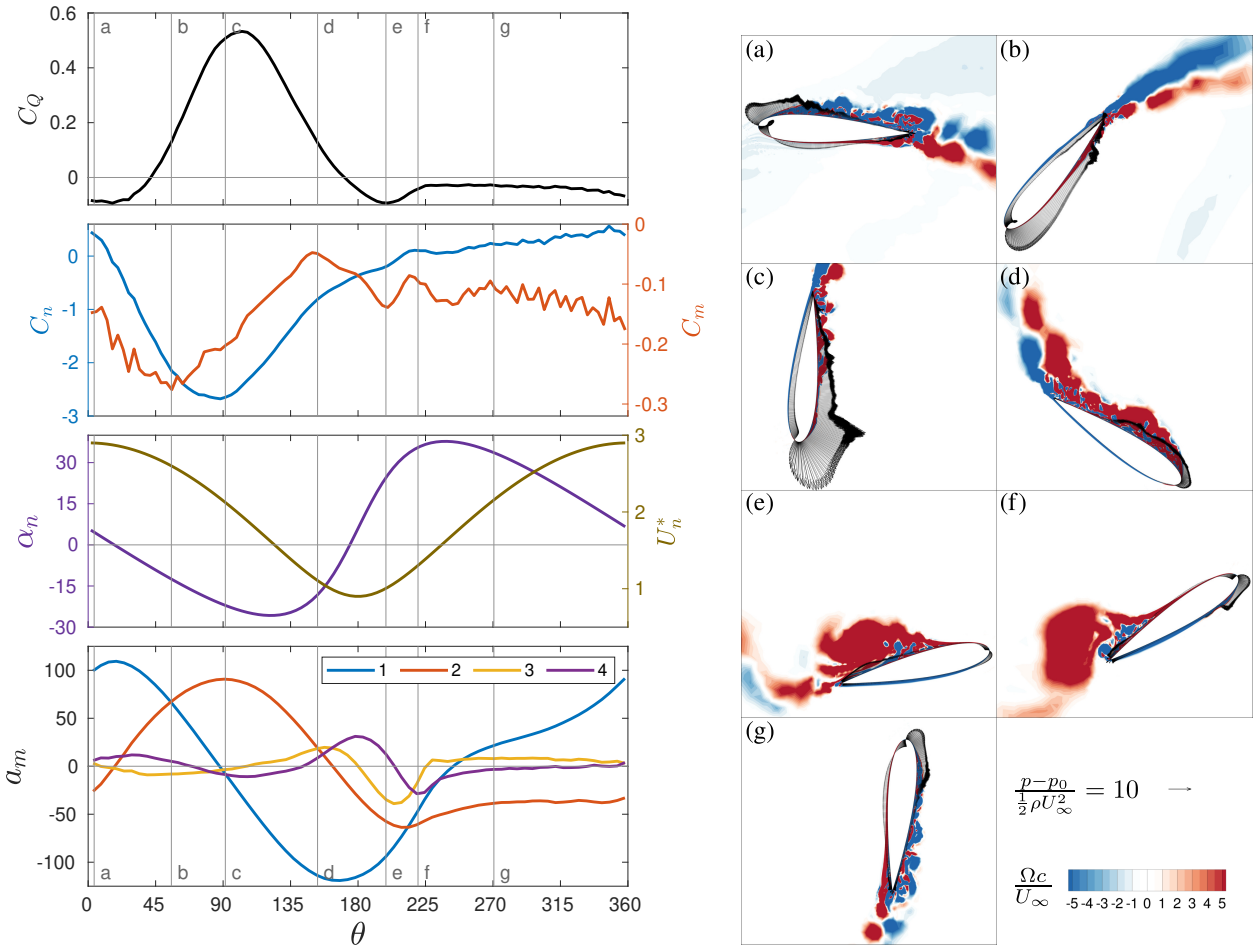

Figure 4.4: **Left:** (Bottom to top) Time development coefficients, nominal relative flow, normal force & pitching moment, and torque generation through a blade rotation. **Right:** Instantaneous surface pressure and vorticity fields.

positive. A low outward normal force acts on the blade due to the partial flow separation on its outer surface during its downstream rotation which also causes an atypical CW or "pitch-up" moment. The angles of attack are lower than the nominal values on the downstream side due to slower oncoming flow. This prevents fully separated flow but is adequate to cause separation and hence loss of suction pressure on only the trailing portion of the outer surface.

During phase (a)-(b), a suction pressure develops on the inside of the blade as observed in Figure 4.4(b) due to the increasing angle of attack, while the flow reattaches on the outside and the mode 2 coefficient surpasses mode 1. As the angle of attack reaches around

12° and the CW pitching moment (pitch-down moment) increases with the lift generation to reach its peak, the flow separates on a small portion near the trailing edge.

A positive pressure develops on the outside of the blade in Figure 4.4(b) and (c) due to reattachment of the boundary layer from the downstream motion. This tends to enhance the inward normal force and the clockwise tendency of the pitching moment. However, the flow separation on the inside at phase (c) results in loss of suction pressure and a CCW pitching moment from the suction at the leading edge, reducing the overall CW moment. The normal force reaches a peak due to the flow separation and the reducing U_n.

During phase (c)-(d), the positive pressure on the outside subsides as the flow is fully reattached. On the inside, the separation point moves towards the leading edge and subsequently an LEV forms concentrating the suction pressure (Figure 4.4(d)). This further reduces the CW moment to its lowest, which coincides with the peak of mode 3 that represents the LEV formation. Beyond (d), the LEV is detached from the leading edge and moves towards the trailing edge, again increasing the CW pitching moment. This is conventionally characterized as the *onset of stall*. Due to the decreasing U_n and flow separation, the normal force continues decreasing after (c).

After (d), the nominal angle of attack rapidly switches side and the LEV convects along the blade (Figure 4.4(e)). A transitional peak is experienced in the CW moment and torque due to the corresponding suction pressure. Notably, apart from mode 3 which accounts for the LEV at the trailing edge, a peak is also observed in mode 2 since it captures reverse flow on the outside of the blade due to the LEV.

Position (f) marks the negative peak of mode 4 as seen in Figure 4.4 which is the instance when the vortex has passed the trailing edge (Figure 4.4(f)). A suction pressure develops at leading edge on the outside causing the pitching moment to remain in the CW direction and the normal force now acting outward from the turbine center.

At phase (g), a partial flow separation can be observed on the outside surface with an

attached flow and suction pressure seen at the leading edge, resulting in a persistent CW pitching moment and a low outward normal force as mentioned for phase (a).

Modal analysis of low TSR, $\lambda = 1.1$

The low tip speed ratio is simulated to explore the physics at high angles of attack and the effectiveness of POD in capturing the dominant features. The first four modes are shown in Figure 4.5. The blade experiences nominal angles of attack up to 60° and a sharp variation in relative velocity as shown in Figure 4.6. Hence a large LEV is created which requires a larger field of view to be included around the blade for the modal decomposition.

Mode 1 represents flow along the blade but involves a rotational flow structure on the inside as opposed to acceleration near the blade seen for $\lambda = 1.9$. Mode 2 shows the flow almost orthogonal to the blade and bending around both the leading and trailing edges. Modes 3 and 4 account for the LEV and its convection from the blade and show the complexity of the vortex dynamics in contrast with the light stall seen for $\lambda = 1.9$. The mode coefficients, nominal relative flow, aerodynamic loads, and flow fields are shown in Figure 4.6. The shape of the pitching moment curve appears similar to the higher λ, however the physics are significantly different as elaborated here for the phases a-g.

Separated flow and vortex shedding is seen at phase (a) in contrast with partial flow separation in $\lambda = 1.9$, while the effective angle of attack at the leading edge appears lower

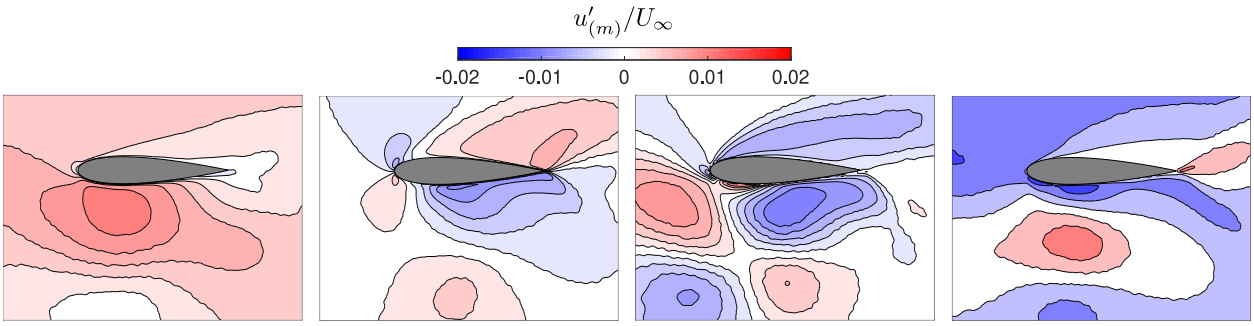

Figure 4.5: Modes as x-velocity fields, for $\lambda = 1.1$.

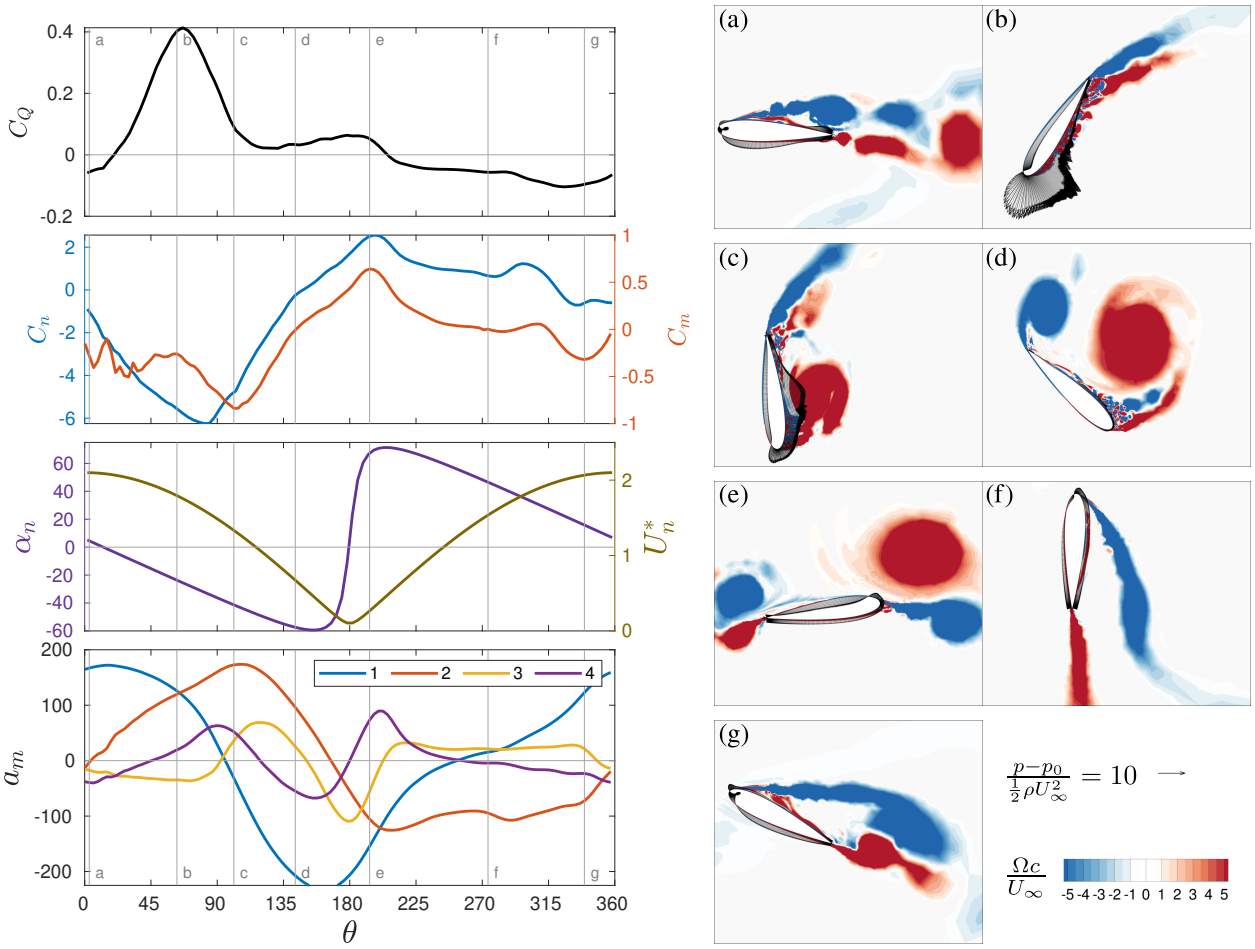

Figure 4.6: **Left:** (Bottom to top) Time development coefficients, nominal relative flow, normal force & pitching moment, and torque generation through a blade rotation. **Right:** Instantaneous surface pressure and vorticity fields.

by observing the point of maximum pressure. A suction pressure is seen developing on the inside that results in a small CW moment that fluctuates beyond (a) due to vortex shedding.

A partial separation is observed on the inside of the blade at (b) due to the sharp increase in angle of attack. Hence the blade does not experience a large CW pitching moment from high lift generation as seen for $\lambda = 1.9$. Instead it directly progresses to an increase in CW moment from flow separation at (c). Due to the high angle of attack, the large stall vortex is formed near the mid-chord rather than the leading edge as also represented by the peak of mode 4 and then mode 3. This increases the CW moment about

the quarter-chord position. As mode 2 surpasses mode 1 at (b), the torque and normal force have nearly reached their peak. From (b)-(c), the torque drops significantly even as mode 2 reaches its peak in contrast with $\lambda = 1.9$ where the peak of mode 2 is correlated with torque. Another contrast is the significance of modes 3 and 4 even as mode 2 continues to be dominant.

The LEV is detached at (d) as it moves away from the blade while inducing an opposite signed trailing edge vortex and the CW moment subsides. As observed at phase (e), the vortex moves across the leading edge and not towards the trailing edge due to the relative flow. Since the relative flow velocity is close to zero, the flow is driven by the vortices. Peculiarly, the leading and trailing edge vortices induce a flow normal into the inside of the blade creating an outward normal force and a CCW pitching moment. Additionally, two weaker vortices are formed at the leading and trailing edges on the outside of the blade due to the complex relative flow induced by the larger vortices on the inside. The complexity can be gauged from the mode coefficients, all of which have comparable values, indicating that all four modes are significant in describing the flow.

As the relative velocity increases from (e)-(f) and the vortices are convected away, a fully separated flow is seen where only mode 2 plays a dominant role. The shear layer from the separating flow at (g) indicates the reduction in angle of attack along with a periodic vortex shedding. The flow continues to be separated until the angle of attack switches side after (a).

4.4 Discussion

Flow curvature effects

The relative flow variation along the chord length of a CFT foil is significant for a high chord-to-radius ratio of 0.47 simulated in this work and is expected to affect the stall dynamics. The streamlines of relative flow in the blade reference frame are concentric

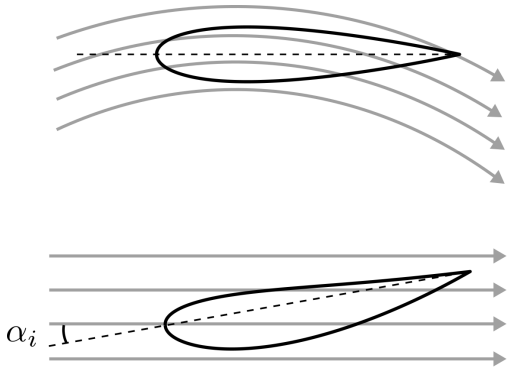

Figure 4.7: Demonstration of virtual camber and incidence due to flow curvature.

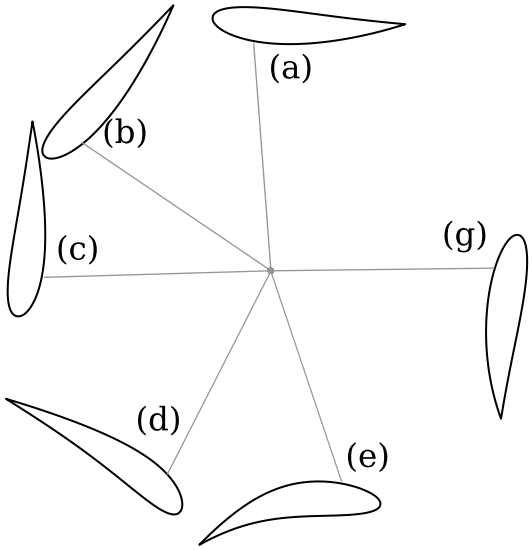

(a) Virtual camber variation corresponding to the positions in Figure 4.4. Chord-to-radius ratio is not to scale.

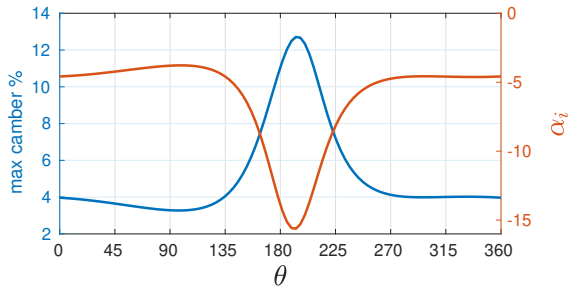

(b) Maximum camber and incidence angle.

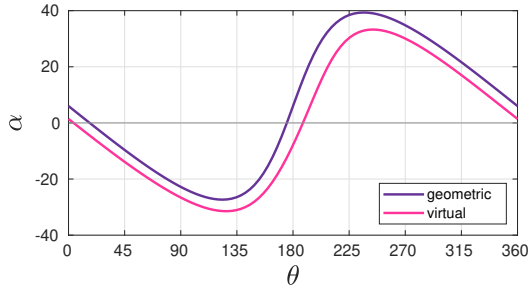

(c) Shift in angle of attack.

Figure 4.8: Flow curvature effects - virtual transformation of the foil computed as per [97] for $\lambda = 1.9$, $c/R = 0.47$, and mounted at the quarter chord location from leading edge.

circles, where the center revolves around the turbine center as a function of the blade's azimuthal position. Migliore et al. [97] perform a conformal mapping of this relative flow to determine an equivalent virtually cambered blade in rectilinear flow as demonstrated in Figure 4.7. This transformation also results in a shift in the incidence angle, α_i, from the geometric angle of attack, α_n. The variation in camber and incidence angle shift of the virtually transformed foil and the resulting virtual angle of attack are shown in Figure 4.8 for $\lambda = 1.9$. The camber and incidence angle follow the trend of the rate of change in α_n (not shown here) though it is not directly proportional. The virtually transformed blade is included in Figure 4.8a at the respective positions from Figure 4.4. The theoretical foil transformation does not account for the gradient of relative velocity along the turbine radius or the flow induction that includes altered oncoming flow on the downstream side. Nevertheless it allows visualizing and predicting the qualitative effect of flow curvature on the outcome.

This effect is manifested in the non-zero fluctuating pitching moment. During the upstream sweep of $\lambda = 1.9$, the virtual camber is positive relative to the angle of attack which is expected to shift the center of pressure towards the trailing edge and hence partly explains the increasing clockwise moment with lift generation until flow separation is seen beyond phase (b). The theoretical camber reaches high values at phase (e) in Figure 4.8b but its effect is difficult to predict since the blade travels through its own wake. As the blade proceeds beyond $\theta = 225°$, the angles of attack are lower than the nominal values due to slower oncoming flow. The incidence angle shift in Figure 4.8c also contributes to the discrepancy between geometric and actual angles of attack which prevents fully separated flow. The relative flow incidence is however adequately high to cause separation and hence loss of suction pressure on only the trailing portion of the outer surface. It is hypothesized that the *negative virtual camber* relative to angle of attack exacerbates this separation behavior. For $\lambda = 1.1$, the deep stall and large induction effects dominate the flow and hence the virtual camber and incidence are expected to have a minimal impact.

History effects and flow induction

History or dynamic effects refers to the flow state, say boundary layer physics, at a specific instance being a function of the system trajectory rather than simply the conditions imposed at that instance. Flow induction here refers to the flow structure and field induced by the blade itself or another blade affecting the instantaneous state. The interaction between these two phenomena are highlighted here.

For $\lambda = 1.9$, the positive pressure during reattachment of the boundary layer on the outer surface at phases (b) and (c) in Figure 4.4 contributes to the clockwise moment in addition to the virtual camber. This phenomenon has been observed in literature for pitching foils too, causing the normal force and pitching moment to cross their static values for the minimum angle of attack during the pitch-down and reattachment [28,85]. However, this is in contrast with negligible pressure during reattachment on the inside in Figure 4.4(f) as a consequence of the low relative velocities, and demonstrates the distinct history effects between the upstream and downstream stroke due to rotation and flow induction.

Phases (e) to (a) in Figure 4.4 reveal that LEV formation or fully separated flow is prevented on the outside due to lower angles of attack. Notably, a fully attached flow with considerable lift generation similar to phase (a)-(b) on the upstream side is never seen on the downstream side. This again is a result of flow induction as the low angle of attack phase (e) involves the foil traveling through its own wake and hence very low relative flow. The angle of attack then rapidly increases to induce partial separation as the true relative flow rises to show an observable effect. Even as the angle of attack tends to reduce again beyond (g), the flow is not reattached until it switches side after (a) because the foil travels through the wake of the other foil and due to flow curvature effects.

Flow induction plays a pivotal role for the $\lambda = 1.1$ rotation as outlined in the previous section, albeit in a distinct manner from the optimal rotation. The stall vortex is larger and stronger and detaches early on in the cycle, impacting the blade loads through a longer span.

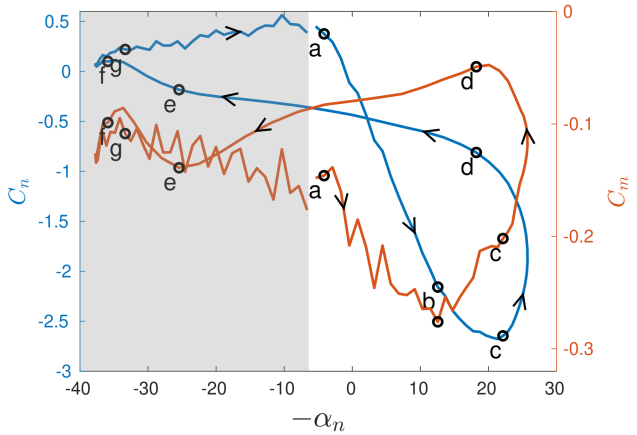

Figure 4.9: Normal force and pitching moment vs nominal angle of attack for $\lambda = 1.9$.

Comparison with non-rotating foils

The aerodynamic loads are plotted in terms of the instantaneous nominal angle of attack in Figure 4.9 to produce a conventional stall loop for the optimal rotation rate. The grey area represents downstream rotation of the turbine where the nominal angle of attack significantly misrepresents the true relative flow. While the nominal value has inaccuracies on the upstream side too, it is expected to closely follow the true relative flow and hence is utilized to compare the dynamic stall loop with prior research. The stall cycle for the normal force creates the typical eight-figure, though the values are negative-biased due to the preset pitch angle, and the cycle in the greyed area is not a mirror image of the upstream cycle despite the nominal relative flow indicating such a profile. In contrast to a pitching foil, the drop in normal force at phase (c) is disassociated from the onset of stall at phase (d) due to the varying relative velocity among other factors.

As seen in literature on pitching and plunging foils [28,91,93], the detachment of LEV, marked by the peak of the LEV mode, causes a “pitch-down" moment onward from phase (d). However, non-rotating blades experience a near-constant pitching moment before the detachment of LEV as compared to the fluctuation after detachment. In contrast, the CFT blade first undergoes an increased pitch-down moment due to the virtual camber effect during attached flow and a positive pressure associated with reattachment on the outside.

This is followed by a reduced CW moment due to flow separation and LEV formation. The pitching moment remains CW (pitch-up) on the downstream side because a fully attached flow or fully separated flow is prevented. The effective “pitch-down" motion, that is, the decrease in nominal angle of attack begins before reaching phase (d) as apparent from Figure 4.9. Following the definition of light and deep stall based on the instance of stall onset relative to start of the pitch-down motion [28], this optimal TSR kinematics can be characterized as experiencing *light stall*.

For $\lambda = 1.1$, due to the complex flow physics, the stall events or evolution of loads are not easily correlated with the modal coefficients. The use of vorticity for performing modal analysis similar to the research by Le Fouest et al. [29] may be more effective in capturing the deep stall events. The detachment of the stall vortex occurs much before the start of the “pitch-down" motion and hence this kinematics can be said to be undergoing a deep stall. However, unlike a pitching or plunging foil, this stall vortex remains in the vicinity of the blade and induces other vortices along with transitional peaks in the pitching moment.

4.5 Conclusions

Proper orthogonal decomposition of the velocity field from LES of a cross-flow turbine reveals a correlation with aerodynamic loads and critical events in the dynamic stall cycle on the blade. The two most energetic modes and their time development coefficients primarily represent the relative velocity magnitude and the lift generation. The third and fourth modes account for the stall vortex formation and shedding.

At the optimal rotation rate, virtual camber due to flow curvature and boundary layer reattachment from the downstream motion of the blade cause a peak in the “pitch-down" moment before the formation and detachment of the leading edge vortex. These events are captured by the relative significance or peaks of the mode coefficients. Flow induction plays a prominent role during the downstream motion as the blade travels through its own

wake and then through low velocity oncoming flow, resulting in an asymmetry from the upstream motion.

For the low rotation rate turbine blade experiencing deep stall, blade-vortex interactions are dominant and responsible for fluctuations in the pitching moment. The correlation of velocity-based mode coefficients with the stall cycle and aerodynamic loads is weaker.

Although the specific outcomes are a function of the two-bladed turbine geometry with a high chord-to-radius ratio of 0.47, they illustrate the complexity of modeling a cross-flow turbine. The modal decomposition acts as a potential guide to designing active flow control measures at the blade. The modes representing reverse flow on the suction side can be used to determine the activation of local boundary layer control mechanisms such as plasma actuation. Although the full velocity field provides information about reverse flow, the modal analysis identifies instances when flow separation gains prominence over lift generation.

5 Intracycle control of angular velocity

5.1 Literature review: control of dynamic stall

In attempts to mitigate dynamic stall, flow control techniques may be used to subdue flow separation on the turbine blades. Passive control solutions such as serrations on the leading edge [116], or a cavity or dimple on the suction surface [117] have been performed, showing moderate improvement by suppressing or delaying flow separation. Active control such as oscillating flaps [118], synthetic jets [119,120], plasma actuators [121], and boundary layer suction [122] have also been investigated, often yielding more enhancement in power than passive control, but these mechanisms are costly to integrate and maintain.

Careful control of the α_n profile is an approach to control the LEV and other unsteady flow mechanisms associated with the dynamic stall process. Equation 1.2 demonstrates how variation of the angle of attack during circular rotation can be controlled through control of either $\alpha_p(\theta)$ or $\lambda(\theta)$. Intracycle variation of the blade pitch angle, α_p, has been previously explored through design and theoretical performance analyses [123–125], experiments [126,127], and simulation [33,34,56,127]. Most of these investigations indicate a maximum enhancement in turbine power of at least 25%, especially for low tip speed ratio values. However, both active and passive pitch control require additional complex mechanisms to be integrated in the design, which drives up turbine cost.

This work investigates an alternative method proposed by Strom et al. [15] who implemented intracycle variation of the angular velocity, ω (and hence, λ) to change the angle of attack and relative flow velocity profiles in equations. 1.2 and 1.3. POD modes that act as a common basis are computed to directly compare the mode coefficients with constant velocity control and explain the torque enhancement. In actual deployment, the use of this method mandates a real-time control of the intracycle variation of ω based on the changes

in oncoming flow speed and direction. However, the advantage of not requiring a yaw mechanism is maintained.

5.2 Methods

Kinematic parameters

For intracycle variation of angular velocity, ω is made to vary sinusoidally with azimuthal position, given by

$$\omega(\theta) = \overline{\omega} + A_\omega sin(2\theta + \phi_\omega). \tag{5.1}$$

The frequency of ω variation is twice the rotation rate for a two-blade turbine. The performance results for a cross-flow turbine rotating at constant ω with $\lambda = 1.9$ are used as the baseline for comparison as the maximum power extraction occurs in this range of tip speed ratio for the confined flow configuration [16]. Hence for the purpose of this investigation, $\overline{\omega}$ is fixed at a value corresponding to $\lambda = 1.9$. The amplitude is set as $A_\omega = 0.63\,\overline{\omega}$, and the phase shift as $\phi_\omega = 4.0\,\mathrm{rad}$, close to the optimal value arrived at by Strom et al. [15]. In practice, power needs to be applied externally to accelerate and decelerate the rotor in order to generate a sinusoidal variation of ω. This input power is not incorporated in the power coefficient here as it integrates to zero over each phase period [15, 128].

Proper orthogonal decomposition

The effectiveness of modal decomposition lies in its representation of the physical system in terms of a reduced order basis. When comparing separate experiments or simulations, the use of separate basis vectors negates this feature. Hence, *common modes* are computed for the velocities from LES of the $\lambda = 1.9$ and sinusoidal λ kinematics such that the flow fields are compared directly through line plots of the mode coefficients since they share a common basis. This is implemented by concatenating the temporal data columns from

both kinematics along rows of the matrix as if the simulation is continuing in time from one kinematics to the other. However, the velocity data is normalized using the total energy of each kinematics before computing the modes to prevent bias from the different number of snapshots or higher velocities in one of the kinematics. The mode coefficients are re-balanced using the normalization factors after the modes are computed.

5.3 Results and discussion

Figure 5.1 displays the four most energetic modes computed for the two kinematics. The resulting first two modes are qualitatively similar to the modes in Figure 4.3 for the velocity field solely from the $\lambda = 1.9$ simulation. Modes 3 and 4 now include spatial variation on the outside of the blade (upper part of the frame in Figure 5.1) in addition to the inside.

Figure 5.2 compares the kinematics, torque and power generation on the left, and the mode coefficients on the right using dashed lines for constant control and continuous lines for sinusoidal control. The sinusoidal variation in λ (middle left) results in a significant change of the nominal relative flow (bottom left). While U_n^* is in phase with the angular velocity variation, the magnitude reaches zero at $\theta = 180°$. Notably, mode 1 imitates U_n^* along with reduced magnitudes on the downstream side but a phase shift of $45°$ to $70°$ is observed between its coefficient and U_n^* for sinusoidal control. The other modes, particularly modes 3 and 4 account for this discrepancy in the mode 1 variation. This phase

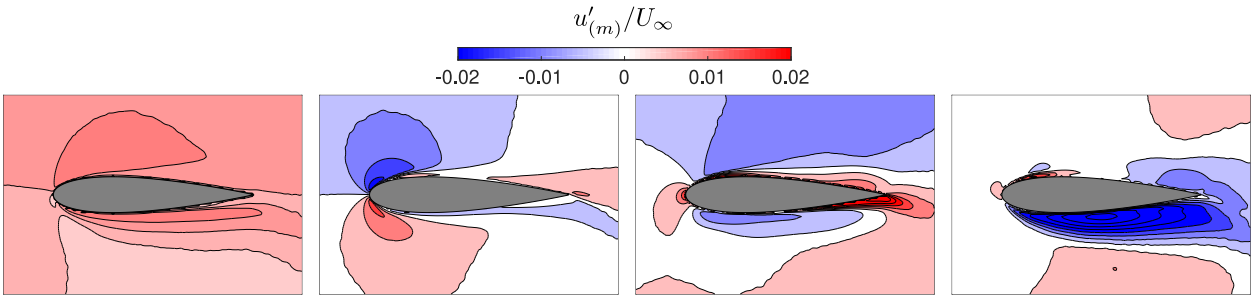

Figure 5.1: Common modes for $\lambda = 1.9$ and sinusoidal λ as x-velocity fields

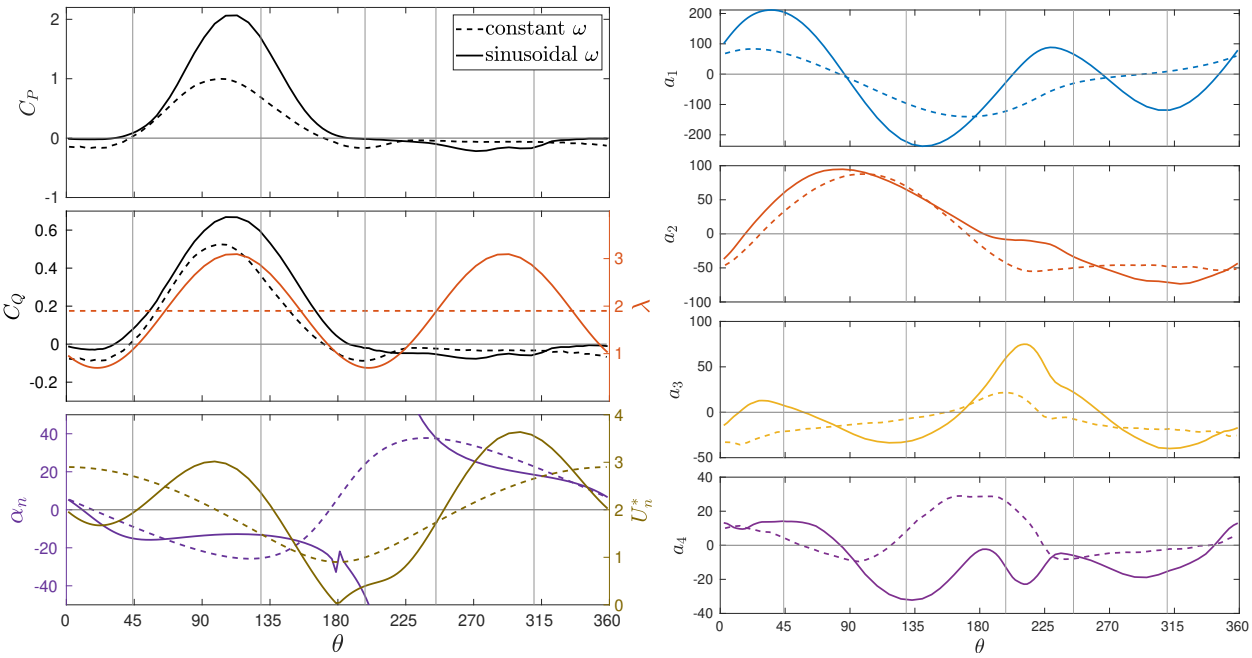

Figure 5.2: **Left:** (Bottom to top) Nominal relative flow and performance of sinusoidal λ compared with $\lambda = 1.9$. **Right:** Temporal mode coefficients for $\lambda = 1.9$ (dashed lines) and sinusoidal λ (continuous lines).

shift is also observed in the independent POD modes from sinusoidal control (not shown here) and emphasizes the need for a careful analysis while drawing physical inferences from a POD-based reduced order model.

The nominal angle of attack rapidly rises to a value of $18°$ and remains almost constant from $\theta = 45°$ to $135°$ for sinusoidal control, in contrast to the continuous variation for constant control (bottom left frame in Figure 5.2). Figure 5.3 demonstrates the nominal relative flow variation through the rotation of a CFT blade for both simulations, superimposed with span-averaged instantaneous vorticity fields from LES. The higher relative flow velocity and lower angle of attack in this azimuthal range is seen to reduce flow separation and delay LEV formation. This delays and increases the peak torque generation for sinusoidal control, plotted in the middle left frame in Figure 5.2. While the mode 2 variation follows the torque generation trend, it does not reproduce this difference between the peak torque for the two kinematics. Finally, the power generation peak, as shown in the top left frame

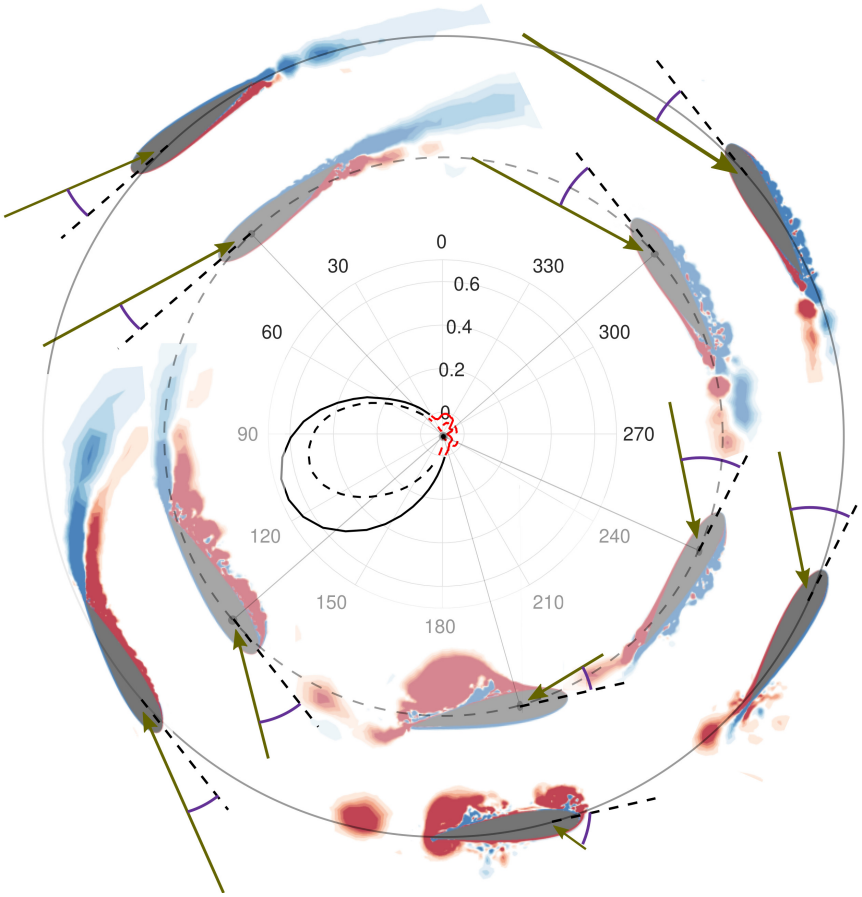

Figure 5.3: Span-averaged vorticity fields compared between sinusoidal control simulation (outer images) and constant control (inner images) at azimuthal positions marked in Figure 5.2. Green vectors and purple angles represent the nominal relative flow velocity. Torque coefficient, C_Q, is reproduced in polar form with the negative values in red color.

in Figure 5.2, is further enhanced as this peak of torque generation aligns with the peak of angular velocity. The average power generation is increased by 40%.

The distinct flow separation manifests prominently in the coefficient for mode 4. As mode 4 in Figure 5.1 displays significant reverse flow on the inner surface, its positive values from $\theta = 120^\circ$ to 220° represent the flow separation and LEV formation for constant control. In contrast, the negative values for sinusoidal control indicate the lack of separation and flow acceleration due to lift generation.

While the distinct LEV on the constant ω blade is seen at $\theta = 200^\circ$ in Figure 5.3, the

sinusoidal ω variation optimizes power generation by delaying stall and produces a trailing edge vortex that sheds the bound vorticity as the angle of attack switches sign. The differences in vortex shedding is represented most prominently by mode 3. The nominal angle of attack for sinusoidal control transitions from one side to another while causing an inverse relative flow on the outside of the blade as represented by higher positive coefficients of mode 3 from $\theta = 180^\circ$ to 270°. Minimal regions of vorticity are seen at $\theta = 245^\circ$ due to this history of low relative flow and drastic angle of attack transition despite the nominal relative flow being identical to that of constant control. Further downstream, the outside surface experiences partial separation similar to that for constant control.

6 Concluding remarks

This research explores multiple aspects of the unsteady flow physics involved in the operation of cross-flow turbines. Although there have been multiple studies on comparing turbulence models, this work compares the high fidelity but expensive LES with low fidelity RANS simulations having a low turn-around time, specifically investigating the effect of confinement. A turbine pair with very high confinement is also simulated using the RANS model. Results show high sensitivity of RANS to the operating conditions, that is, the confinement and the local Reynolds number. It is however able to predict the performance and forces successfully in conditions such as the unconfined configuration and the lower range of tip speed ratios for the turbine pair, indicating its usefulness along with the need to develop more robust models.

Much of the literature on CFT focuses on performance optimization and system level analysis of the flow. With a sharper focus on the dynamic stall cycle, this work analyzes the time evolution of dominant velocity modes around the blade from LES. The modes are able to capture trends in blade aerodynamic loading along with critical events such as the stall vortex formation and shedding. The surface pressure and vorticity field on the blade emphasizes the importance of flow curvature, history effects, and flow induction on the fluctuations in the pitching moment and force, as compared to a non-rotating pitching or plunging blade. In addition, a common basis of modes highlights the delayed flow separation and altered vortex shedding behavior for the sinusoidal intracycle variation of angular velocity that increases power generation by 40% as compared to constant angular velocity control. Hence, the modal analysis can be employed for designing or evaluating separation control mechanisms.

Bibliography

[1] L. Kilcher, M. Fogarty, and M. Lawson, "Marine energy in the united states:an overview of opportunities," tech. rep., National Renewable Energy Laboratory, 2021.

[2] R. Kumar, K. Raahemifar, and A. S. Fung, "A critical review of vertical axis wind turbines for urban applications," *Renewable and Sustainable Energy Reviews*, vol. 89, pp. 281–291, 6 2018.

[3] https://www.businessgreen.com/news/3000806/first-meygen-tidal-turbine-reaches-full-power-off-coast-of-scotland, 2016. [Online; accessed 15-May-2021].

[4] C. R. Sauer and J. McEntee, "Tidgen power system commercialization project," tech. rep., ORPC Maine, 12 2013.

[5] G. Darrieus, "Turbine having its rotating shaft transverse to the flow of the current," 1931.

[6] W. Wacker. Licensed under CC BY-SA 3.0 (https://creativecommons.org/licenses/by-sa/3.0), via Wikimedia Commons.

[7] Sozialutopist. Licensed under CC BY-SA 3.0 (https://creativecommons.org/licenses/by-sa/3.0), via Wikimedia Commons.

[8] J. O. Dabiri, "Potential order-of-magnitude enhancement of wind farm power density via counter-rotating vertical-axis wind turbine arrays," *Journal of Renewable and Sustainable Energy*, vol. 3, 7 2011.

[9] I. Paraschivoiu, *Wind turbine design: with emphasis on Darrieus concept*. Presses inter Polytechnique, 2002.

[10] J. H. Strickland, B. T. Webster, and T. Nguyen, "A vortex model of the darrieus turbine: An analytical and experimental study," *Journal of Fluids Engineering, Transactions of the ASME*, vol. 101, pp. 500–505, 12 1979.

[11] R. E. Wilson and S. N. Walker, "Fixed-wake analysis of the darrieus rotor," tech. rep., Sandia National Labs.; Oregon State Univ, 1981.

[12] J. N. Sørensen and W. Z. Shen, "Numerical modeling of wind turbine wakes," *Journal of Fluids Engineering, Transactions of the ASME*, vol. 124, pp. 393–399, 6 2002.

[13] W. Z. Shen, J. H. Zhang, and J. N. Sørensen, "The actuator surface model: A new navier-stokes based model for rotor computations," *Journal of Solar Energy Engineering, Transactions of the ASME*, vol. 131, pp. 0110021–0110029, 2 2009.

[14] H. C. Tsai and T. Colonius, "Coriolis effect on dynamic stall in a vertical axis wind turbine," *AIAA Journal*, vol. 54, pp. 216–226, 9 2016.

[15] B. Strom, S. L. Brunton, and B. Polagye, "Intracycle angular velocity control of cross-flowăturbines," *Nature Energy*, vol. 2, pp. 1–9, 2017.

[16] A. Snortland, B. Polagye, and O. Williams, "Influence of near-blade hydrodynamics on cross-flow turbine performance," in *Proceedings of the 13th European Wave and Tidal Energy Conference*, pp. 1–9, 2019.

[17] T. Kinsey and G. Dumas, "Impact of channel blockage on the performance of axial and cross-flow hydrokinetic turbines," *Renewable Energy*, vol. 103, pp. 239–254, 4 2017.

[18] H. Ross and B. Polagye, "An experimental assessment of analytical blockage corrections for turbines," *Renewable Energy*, vol. 152, pp. 1328–1341, 6 2020.

[19] C. A. Consul, R. H. Willden, and S. C. McIntosh, "Blockage effects on the hydrodynamic performance of a marine cross-flow turbine," *Philosophical Transactions of the Royal Society A: Mathematical, Physical and Engineering Sciences*, vol. 371, 2 2013.

[20] O. Gauvin-Tremblay and G. Dumas, "Two-way interaction between river and deployed cross-flow hydrokinetic turbines," *Journal of Renewable and Sustainable Energy*, vol. 12, p. 034501, 5 2020.

[21] A. Hunt, C. Stringer, and B. Polagye, "Effect of aspect ratio on cross-flow turbine performance," *Journal of Renewable and Sustainable Energy*, vol. 12, p. 054501, 9 2020.

[22] W. Timmer, "Two-dimensional low-reynolds number wind tunnel results for airfoil naca 0018," *Wind Engineering*, vol. 32, pp. 525–537, 12 2008.

[23] B. K. Kirke and L. Lazauskas, "Limitations of fixed pitch darrieus hydrokinetic turbines and the challenge of variable pitch," *Renewable Energy*, vol. 36, pp. 893–897, 3 2011.

[24] E. Möllerström, P. Gipe, J. Beurskens, and F. Ottermo, "A historical review of vertical axis wind turbines rated 100 kw and above," *Renewable and Sustainable Energy Reviews*, vol. 105, pp. 1–13, 5 2019.

[25] N. Fujisawa and S. Shibuya, "Observations of dynamic stall on turbine blades," *Journal of Wind Engineering and Industrial Aerodynamics*, vol. 89, pp. 201–214, 2 2001.

[26] C. S. Ferreira, G. van Kuik, G. van Bussel, and F. Scarano, "Visualization by piv of dynamic stall on a vertical axis wind turbine," *Experiments in Fluids*, vol. 46, pp. 97–108, 1 2009.

[27] Y. Wang, X. Sun, B. Zhu, H. Zhang, and D. Huang, "Effect of blade vortex interaction on performance of darrieus-type cross flow marine current turbine," *Renewable Energy*, vol. 86, pp. 316–323, 2 2016.

[28] K. Mulleners and M. Raffel, "The onset of dynamic stall revisited," *Experiments in Fluids*, vol. 52, pp. 779–793, 3 2012.

[29] S. L. Fouest, D. Fernex, and K. Mulleners, "Timescales of dynamic stall development on a vertical-axis wind turbine blade," *arXiv:2210.16259*, 10 2022.

[30] R. I. Issa, "Solution of the implicitly discretised fluid flow equations by operator-splitting," *Journal of computational physics*, vol. 62, no. 1, pp. 40–65, 1986.

[31] H. G. Weller, G. Tabor, H. Jasak, and C. Fureby, "A tensorial approach to computational continuum mechanics using object-oriented techniques," *Computers in physics*, vol. 12, no. 6, pp. 620–631, 1998.

[32] F. R. Menter, "Two-equation eddy-viscosity turbulence models for engineering applications," *AIAA journal*, vol. 32, no. 8, pp. 1598–1605, 1994.

[33] R. Gosselin, M. Boudreau, and G. Dumas, "Parametric study of h-darrieus vertical-axis turbines using urans simulations," in *21st Annual Conference of the CFD Society of Canada*, CFD Society of Canada, 2013.

[34] B. Paillard, J. Astolfi, and F. Hauville, "Uranse simulation of an active variable-pitch cross-flow darrieus tidal turbine: Sinusoidal pitch function investigation," *International Journal of Marine Energy*, vol. 11, pp. 9–26, 9 2015.

[35] F. Balduzzi, A. Bianchini, R. Maleci, G. Ferrara, and L. Ferrari, "Critical issues in the cfd simulation of darrieus wind turbines," *Renewable Energy*, vol. 85, pp. 419–435, 2016.

[36] B. Hand, G. Kelly, and A. Cashman, "Numerical simulation of a vertical axis wind turbine airfoil experiencing dynamic stall at high reynolds numbers," *Computers and Fluids*, vol. 149, pp. 12–30, 6 2017.

[37] K. H. Wong, W. T. Chong, N. L. Sukiman, Y.-C. Shiah, S. C. Poh, K. Sopian, and W.-C. Wang, "Experimental and simulation investigation into the effects of a flat plate deflector on vertical axis wind turbine," *Energy Conversion and Management*, vol. 160, pp. 109–125, 3 2018.

[38] K. Rogowski, M. O. L. Hansen, and R. Maroski, "Steady and unsteady analysis of naca 0018 airfoil in vertical-axis wind turbine," *Journal of Theoretical and Applied Mechanics*, vol. 56, p. 203, 1 2018.

[39] M. R. Castelli, G. Ardizzon, L. Battisti, E. Benini, and G. Pavesi, "Modeling strategy and numerical validation for a darrieus vertical axis micro-wind turbine," in *ASME International Mechanical Engineering Congress and Exposition, Proceedings (IMECE)*, pp. 1–10, 2010.

[40] J. E. Bardina, P. G. Huang, and T. J. Coakley, "Turbulence modeling validation, testing, and development," tech. rep., NASA Ames Research Center, 1997.

[41] L. Daróczy, G. Janiga, K. Petrasch, M. Webner, and D. Thévenin, "Comparative analysis of turbulence models for the aerodynamic simulation of h-darrieus rotors," *Energy*, vol. 90, pp. 680–690, 10 2015.

[42] F. Menter and T. Esch, "Elements of Industrial Heat Transfer Predictions," in *16th Brazilian Congr. Mech. Eng.*, pp. 117–127, 2001.

[43] M. J. Barnsley and J. F. Wellicome, "Final report on the 2nd phase of development and testing of a horizontal axis wind turbine test rig for the investigation of stall regulation aerodynamics," tech. rep., ETSU, 1990.

[44] J. Zhou, R. J. Adrian, S. Balachandar, and T. M. Kendall, "Mechanisms for generating coherent packets of hairpin vortices in channel flow," *J. Fluid Mech.*, vol. 387, pp. 353–396, may 1999.

[45] R. J. Adrian, K. T. Christensen, and Z.-C. Liu, "Analysis and interpretation of instantaneous turbulent velocity fields," *Exp. Fluids*, vol. 29, pp. 275–290, sep 2000.

[46] W. W. Kim and S. Menon, "A new dynamic one-equation subgrid-scale model for large eddy simulations," in *33rd Aerosp. Sci. Meet. Exhib.*, American Institute of Aeronautics and Astronautics Inc, AIAA, 1995.

[47] A. Yoshizawa, "Statistical theory for compressible turbulent shear flows, with the application to subgrid modeling.," *PHYS. FLUIDS*, vol. 29, pp. 2152–2164, jun 1986.

[48] J. Smagorinsky, "General circulation experiments with the primitive equations," *Mon. Weather Rev.*, vol. 91, pp. 99–164, mar 1963.

[49] F. Nicoud and F. Ducros, "Subgrid-scale stress modelling based on the square of the velocity gradient tensor," *Flow, Turbul. Combust.*, vol. 62, no. 3, pp. 183–200, 1999.

[50] E. R. Van Driest, "On Turbulent Flow Near a Wall," *J. Aeronaut. Sci.*, vol. 23, pp. 1007–1011, nov 1956.

[51] S. Kim, P. A. Wilson, and Z. M. Chen, "Effect of turbulence modelling on 3-D LES of transitional flow behind a circular cylinder," *Ocean Eng.*, vol. 100, pp. 19–25, may 2015.

[52] Z. Feng, H. Qi, X. Huang, S. Liu, and J. Liu, "Comparisons of Subgrid-Scale Models for OpenFoam Large- Eddy Simulation," in *IOP Conf. Ser. Earth Environ. Sci.*, vol. 1802, p. 42088, IOP Publishing Ltd, mar 2021.

[53] H. Lu, C. J. Rutland, and L. M. Smith, "A priori tests of one-equation LES modeling of rotating turbulence," *J. Turbul.*, vol. 8, no. 37, pp. 1–27, 2007.

[54] E. Amet, T. Maître, C. Pellone, and J. L. Achard, "2d numerical simulations of blade-vortex interaction in a darrieus turbine," *Journal of Fluids Engineering, Transactions of the ASME*, vol. 131, pp. 1–15, 11 2009.

[55] S. Wang, D. B. Ingham, L. Ma, M. Pourkashanian, and Z. Tao, "Numerical investigations on dynamic stall of low reynolds number flow around oscillating airfoils," *Computers and Fluids*, vol. 39, pp. 1529–1541, 10 2010.

[56] G. Abdalrahman, W. Melek, and F.-S. Lien, "Pitch angle control for a small-scale darrieus vertical axis wind turbine with straight blades (h-type vawt)," *Renewable Energy*, vol. 114, pp. 1353–1362, 12 2017.

[57] C. J. S. Ferreira, A. van Zuijlen, H. Bijl, G. van Bussel, and G. van Kuik, "Simulating dynamic stall in a two-dimensional vertical-axis wind turbine: verification and validation with particle image velocimetry data," *Wind Energy*, vol. 13, pp. 1–17, 1 2010.

[58] A. J. Buchner, M. W. Lohry, L. Martinelli, J. Soria, and A. J. Smits, "Dynamic stall in vertical axis wind turbines: Comparing experiments and computations," *Journal of Wind Engineering and Industrial Aerodynamics*, vol. 146, pp. 163–171, 11 2015.

[59] J. McNaughton, F. Billard, and A. Revell, "Turbulence modelling of low reynolds number flow effects around a vertical axis turbine at a range of tip-speed ratios," *Journal of Fluids and Structures*, vol. 47, pp. 124–138, 5 2014.

[60] R. Howell, N. Qin, J. Edwards, and N. Durrani, "Wind tunnel and numerical study of a small vertical axis wind turbine," *Renewable Energy*, vol. 35, pp. 412–422, 2 2010.

[61] P. Bachant and M. Wosnik, "Modeling the near-wake of a vertical-axis cross-flow turbine with 2-d and 3-d rans," *Journal of Renewable and Sustainable Energy*, vol. 8, p. 053311, 9 2016.

[62] H. Lam and H. Peng, "Study of wake characteristics of a vertical axis wind turbine by two- and three-dimensional computational fluid dynamics simulations," *Renewable Energy*, vol. 90, pp. 386–398, 5 2016.

[63] S. Yagmur and F. Kose, "Numerical evolution of unsteady wake characteristics of h-type darrieus hydrokinetic turbine for a hydro farm arrangement," *Applied Ocean Research*, vol. 110, p. 102582, 5 2021.

[64] C. Li, S. Zhu, Y. lin Lin Xu, and Y. Xiao, "2.5d large eddy simulation of vertical axis wind turbine in consideration of high angle of attack flow," *Renewable Energy*, vol. 51, pp. 317–330, 3 2013.

[65] J. He, X. Jin, S. Xie, L. Cao, Y. Wang, Y. Lin, and N. Wang, "Cfd modeling of varying complexity for aerodynamic analysis of h-vertical axis wind turbines," *Renewable Energy*, vol. 145, pp. 2658–2670, 1 2020.

[66] H. Lei, D. Zhou, Y. Bao, Y. Li, and Z. Han, "Three-dimensional improved delayed detached eddy simulation of a two-bladed vertical axis wind turbine," *Energy Conversion and Management*, vol. 133, pp. 235–248, 2 2017.

[67] O. Mejia, J. Quiñones, and S. Laín, "Rans and hybrid rans-les simulations of an h-type darrieus vertical axis water turbine," *Energies*, vol. 11, p. 2348, 9 2018.

[68] P. Ouro and T. Stoesser, "An immersed boundary-based large-eddy simulation approach to predict the performance of vertical axis tidal turbines," *Computers and Fluids*, vol. 152, pp. 74–87, 7 2017.

[69] M. Kinzel, Q. Mulligan, and J. O. Dabiri, "Energy exchange in an array of vertical-axis wind turbines," *Journal of Turbulence*, vol. 13, pp. 1–13, 2012.

[70] V. Rolin and F. Porté-Agel, "Wind-tunnel study of the wake behind a vertical axis wind turbine in a boundary layer flow using stereoscopic particle image velocimetry," *Journal of Physics: Conference Series*, vol. 625, p. 012012, 6 2015.

[71] K. J. Ryan, F. Coletti, J. O. Dabiri, and J. K. Eaton, "Three-dimensional velocity measurements around and downstream of a rotating vertical axis wind turbine," in *Proceedings of the ASME Turbo Expo*, vol. 3B, American Society of Mechanical Engineers (ASME), 2014.

[72] G. Tescione, D. Ragni, C. He, C. J. S. Ferreira, and G. J. van Bussel, "Near wake flow analysis of a vertical axis wind turbine by stereoscopic particle image velocimetry," *Renewable Energy*, vol. 70, pp. 47–61, 10 2014.

[73] B. Strom, B. Polagye, and S. L. Brunton, "Near-wake dynamics of a vertical-axis turbine," *Journal of Fluid Mechanics*, vol. 935, p. A6, 3 2022.

[74] L. Battisti, L. Zanne, S. Dell'Anna, V. Dossena, G. Persico, and B. Paradiso, "Aerodynamic measurements on a vertical axis wind turbine in a large scale wind tunnel," *Journal of Energy Resources Technology, Transactions of the ASME*, vol. 133, 2011.

[75] H. Y. Peng and H. F. Lam, "Turbulence effects on the wake characteristics and aerodynamic performance of a straight-bladed vertical axis wind turbine by wind tunnel tests and large eddy simulations," *Energy*, vol. 109, pp. 557–568, 8 2016.

[76] N. J. Wei, I. D. Brownstein, J. L. Cardona, M. F. Howland, and J. O. Dabiri, "Near-wake structure of full-scale vertical-axis wind turbines," *Journal of Fluid Mechanics*, vol. 914, p. 17, 2021.

[77] A. Posa, "Secondary flows in the wake of a vertical axis wind turbine of solidity 0.5 working at a tip speed ratio of 2.2," *Journal of Wind Engineering and Industrial Aerodynamics*, vol. 213, 6 2021.

[78] A. Posa, C. M. Parker, M. C. Leftwich, and E. Balaras, "Wake structure of a single vertical axis wind turbine," *International Journal of Heat and Fluid Flow*, vol. 61, pp. 75–84, 10 2016.

[79] F. Scheurich and R. E. Brown, "Effect of dynamic stall on the aerodynamics of vertical-axis wind turbines," *AIAA Journal*, vol. 49, pp. 2511–2521, 2011.

[80] S. Shamsoddin and F. Porté-Agel, "Large eddy simulation of vertical axis wind turbine wakes," *Energies*, vol. 7, pp. 890–912, 2 2014.

[81] M. Abkar and J. O. Dabiri, "Self-similarity and flow characteristics of vertical-axis wind turbine wakes: an les study," *Journal of Turbulence*, vol. 18, pp. 373–389, 4 2017.

[82] M. Grondeau, S. Guillou, P. Mercier, and E. Poizot, "Wake of a ducted vertical axis tidal turbine in turbulent flows, lbm actuator-line approach," *Energies*, vol. 12, p. 4273, 11 2019.

[83] V. Mendoza, P. Bachant, C. Ferreira, and A. Goude, "Nearwake flow simulation of a vertical axis turbine using an actuator line model," *Wind Energy*, vol. 22, pp. 171–188, 2 2019.

[84] M. Dave, B. Strom, A. Snortland, O. Williams, B. Polagye, and J. A. Franck, "Simulations of intracycle angular velocity control for a crossflow turbine," *AIAA Journal*, vol. 59, pp. 812–824, 3 2021.

[85] L. W. Carr, "Progress in analysis and prediction of dynamic stall," *https://doi.org/10.2514/3.45534*, vol. 25, pp. 6–17, 5 1988.

[86] W. Sheng, R. A. D. Galbraith, and F. N. Coton, "A new stall-onset criterion for low speed dynamic-stall," *Journal of Solar Energy Engineering*, vol. 128, pp. 461–471, 11 2006.

[87] D. G. Coleman, F. O. Thomas, S. Gordeyev, and T. C. Corke, "Parametric modal decomposition of dynamic stall," *https://doi.org/10.2514/1.J057077*, vol. 57, pp. 176–190, 11 2018.

[88] M. Ramasamy, A. Sanayei, J. S. Wilson, P. B. Martin, T. Harms, P. Nikoueeyan, and J. Naughton, "Reducing uncertainty in dynamic stall measurements through data-driven clustering of cycle-to-cycle variations," *Journal of the American Helicopter Society*, vol. 66, pp. 1–17, 11 2020.

[89] F. O. Carta, "a comparison of the pitching and plunging response of an oscillating airfoil," tech. rep., United Technologies Research Center, Prepared for Langley Research Center, NASA, 10 1979.

[90] J. G. Wong, A. Mohebbian, J. Kriegseis, and D. E. Rival, "Rapid flow separation for transient inflow conditions versus accelerating bodies: An investigation into their equivalency," *Journal of Fluids and Structures*, vol. 40, pp. 257–268, 7 2013.

[91] D. Kim, B. Strom, S. Mandre, and K. Breuer, "Energy harvesting performance and flow structure of an oscillating hydrofoil with finite span," *Journal of Fluids and Structures*, vol. 70, pp. 314–326, 4 2017.

[92] J. A. Franck and K. S. Breuer, "Unsteady high-lift mechanisms from heaving flat plate simulations," *International Journal of Heat and Fluid Flow*, vol. 67, pp. 230–239, 2017.

[93] B. L. R. Ribeiro, S. L. Frank, and J. A. Franck, "Vortex dynamics and reynolds number effects of an oscillating hydrofoil in energy harvesting mode," *Journal of Fluids and Structures*, vol. 94, p. 102888, 4 2020.

[94] M. Dave, A. Spaulding, and J. A. Franck, "Variable thrust and high efficiency propulsion with oscillating foils at high reynolds numbers," *Ocean Engineering*, vol. 214, p. 107833, 10 2020.

[95] R. Dunne and B. J. McKeon, "Dynamic stall on a pitching and surging airfoil," *Experiments in Fluids*, vol. 56, p. 157, 8 2015.

[96] K. Gharali and D. A. Johnson, "Dynamic stall simulation of a pitching airfoil under unsteady freestream velocity," *Journal of Fluids and Structures*, vol. 42, pp. 228–244, 10 2013.

[97] P. G. Migliore, W. P. Wolfe, and J. B. Fanucci, "Flow curvature effects on darrieus turbine blade aerodynamics," *Journal of Energy*, vol. 4, pp. 49–55, 3 1980.

[98] A. Bianchini, E. A. Carnevale, and L. Ferrari, "A model to account for the virtual camber effect in the performance prediction of an h-darrieus vawt using the momentum models," *Wind Engineering*, vol. 35, pp. 465–482, 8 2011.

[99] F. Balduzzi, A. Bianchini, R. Maleci, G. Ferrara, and L. Ferrari, "Blade design criteria to compensate the flow curvature effects in h-darrieus wind turbines," *Journal of Turbomachinery*, vol. 137, 1 2014.

[100] J. M. Rainbird, A. Bianchini, F. Balduzzi, J. Peiró, J. M. R. Graham, G. Ferrara, and L. Ferrari, "On the influence of virtual camber effect on airfoil polars for use in simulations of darrieus wind turbines," *Energy Conversion and Management*, vol. 106, pp. 373–384, 12 2015.

[101] A. Bianchini, F. Balduzzi, G. Ferrara, and L. Ferrari, "Virtual incidence effect on rotating airfoils in darrieus wind turbines," *Energy Conversion and Management*, vol. 111, pp. 329–338, 3 2016.

[102] S. V. D. Horst, J. V. D. Wiel, C. S. Ferreira, and N. R. García, "Flow curvature effects for vawt: A review of virtual airfoil transformations and implementation in xfoil," *34th Wind Energy Symposium*, 2016.

[103] A. Bianchini, F. Balduzzi, G. Ferrara, and L. Ferrari, "Aerodynamics of darrieus wind turbines airfoils: The impact of pitching moment," *Journal of Engineering for Gas Turbines and Power*, vol. 139, 4 2017.

[104] S. Mariappan, A. D. Gardner, K. Richter, and M. Raffel, "Analysis of dynamic stall using dynamic mode decomposition technique," *AIAA Journal*, vol. 52, pp. 2427–2439, 11 2014.

[105] A. T. Mohan, D. V. Gaitonde, and M. R. Visbal, "Model reduction and analysis of deep dynamic stall on a plunging airfoil," *Computers and Fluids*, vol. 129, pp. 1–19, 4 2016.

[106] J. Seidel, S. Siegel, K. Cohen, and T. McLaughlin, "Pod based separation control on the naca0015 airfoil," *43rd AIAA Aerospace Sciences Meeting and Exhibit - Meeting Papers*, pp. 12059–12069, 2005.

[107] A. T. Mohan and D. V. Gaitonde, "Analysis of airfoil stall control using dynamic mode decomposition," *https://doi.org/10.2514/1.C034044*, vol. 54, pp. 1508–1520, 2 2017.

[108] K. Taira, M. S. Hemati, S. L. Brunton, Y. Sun, K. Duraisamy, S. Bagheri, S. T. Dawson, and C. A. Yeh, "Modal analysis of fluid flows: Applications and outlook," *AIAA Journal*, vol. 58, pp. 998–1022, 10 2020.

[109] I. Scherl, *Optimization, Modeling, and Control of Cross-Flow Turbine Arrays*. PhD thesis, University of Washington, 2022.

[110] M. Mohamed, A. Ali, and A. Hafiz, "Cfd analysis for h-rotor darrieus turbine as a low speed wind energy converter," *Engineering Science and Technology, an International Journal*, vol. 18, pp. 1–13, 3 2015.

[111] L. Daróczy, G. Janiga, and D. Thévenin, "Computational fluid dynamics based shape optimization of airfoil geometry for an h-rotor using a genetic algorithm," *Engineering Optimization*, vol. 50, pp. 1483–1499, 9 2018.

[112] V. Patel, T. I. Eldho, and S. V. Prabhu, "Experimental investigations on darrieus straight blade turbine for tidal current application and parametric optimization for hydro farm arrangement," *International Journal of Marine Energy*, vol. 17, pp. 110–135, 4 2017.

[113] I. Scherl, B. Strom, S. L. Brunton, and B. L. Polagye, "Geometric and control optimization of a two cross-flow turbine array," *Journal of Renewable and Sustainable Energy*, vol. 12, p. 064501, 11 2020.

[114] V. Pasumarti, M. Dave, and J. Franck, "Simulation of two cross-flow turbines under confinement," *AIAA AVIATION 2022 Forum*, 2022.

[115] L. Sirovich, "Turbulence and the dynamics of coherent structures. i. coherent structures," *Quarterly of Applied Mathematics*, vol. 45, pp. 561–571, 1987.

[116] Z. Wang and M. Zhuang, "Leading-edge serrations for performance improvement on a vertical-axis wind turbine at low tip-speed-ratios," *Applied Energy*, vol. 208, pp. 1184–1197, 12 2017.

[117] E. Sobhani, M. Ghaffari, and M. J. Maghrebi, "Numerical investigation of dimple effects on darrieus vertical axis wind turbine," *Energy*, vol. 133, pp. 231–241, 8 2017.

[118] Q. Xiao, W. Liu, and A. Incecik, "Flow control for vatt by fixed and oscillating flap," *Renewable Energy*, vol. 51, pp. 141–152, 3 2013.

[119] J. Yen and N. A. Ahmed, "Enhancing vertical axis wind turbine by dynamic stall control using synthetic jets," *Journal of Wind Engineering and Industrial Aerodynamics*, vol. 114, pp. 12–17, 3 2013.

[120] D. Velasco, O. L. Mejia, and S. Laín, "Numerical simulations of active flow control with synthetic jets in a darrieus turbine," *Renewable Energy*, vol. 113, pp. 129–140, 12 2017.

[121] D. Greenblatt, M. Schulman, and A. Ben-Harav, "Vertical axis wind turbine performance enhancement using plasma actuators," *Renewable Energy*, vol. 37, pp. 345–354, 1 2012.

[122] N. Morgulis and A. Seifert, "Fluidic flow control applied for improved performance of darrieus wind turbines," *Wind Energy*, vol. 19, pp. 1585–1602, 9 2016.

[123] A. Schönborn and M. Chantzidakis, "Development of a hydraulic control mechanism for cyclic pitch marine current turbines," *Renewable Energy*, vol. 32, pp. 662–679, 4 2007.

[124] I. Paraschivoiu, O. Trifu, and F. Saeed, "H-darrieus wind turbine with blade pitch control," *International Journal of Rotating Machinery*, vol. 2009, pp. 1–7, 2009.

[125] L. Lazauskas, "Three pitch control systems for vertical axis wind turbines compared," *Wind Engineering*, vol. 16, pp. 269–282, 1992.

[126] B. K. Kirke, "Tests on ducted and bare helical and straight blade darrieus hydrokinetic turbines," *Renewable Energy*, vol. 36, pp. 3013–3022, 2011.

[127] M. Elkhoury, T. Kiwata, and E. Aoun, "Experimental and numerical investigation of a three-dimensional vertical-axis wind turbine with variable-pitch," *Journal of Wind Engineering and Industrial Aerodynamics*, vol. 139, pp. 111–123, 4 2015.

[128] B. Polagye, B. Strom, H. Ross, D. Forbush, and R. J. Cavagnaro, "Comparison of cross-flow turbine performance under torque-regulated and speed-regulated control," *Journal of Renewable and Sustainable Energy*, vol. 11, p. 044501, 7 2019.